Synthesis, Structure, and Electronic Characterization of Reactive Diiron(II) 1,2-Bis(2-hydroxybenzamido)benzene Complexes as Models for Methane Monooxygenase

A. Stassinopoulos,[†] G. Schulte,[†] G. C. Papaefthymiou,[‡] and J. P. Caradonna*,[†]

Contribution from the Kline Chemistry Laboratory, Yale University, New Haven, Connecticut 06511, and the Francis Bitter National Magnet Laboratory, Massachusetts Institute of Technology, Cambridge, Massachusetts 02139. *Received January 25, 1991*

Abstract: The dinuclear iron(II) compound $[Fe_2(H_2Hbab)_2(N\text{-}Melm)_2]$, **10**, and its DMF solvated form, $[Fe_2(H_2Hbab)_2(DMF)_2(N\text{-}Melm)]$, **11** ($H_4Hbab$ = 1,2-bis(2-hydroxybenzamido)benzene), were synthesized, and their structures were determined by X-ray crystallography. Compound **10** crystallizes in triclinic space group $P_{\bar{1}}$ with a = 9.969 (4) Å, b = 12.754 (5) Å, c = 9.919 (7) Å, α = 100.60 (5)°, β = 118.40 (4)°, γ = 77.42 (3)°, and Z = 2. The compound is centrosymmetric with two equivalent $FeNO_4$ trigonal-bipyramidal coordination spheres composed of amide oxygen atoms, terminal and bridging phenolate oxygen atoms, and a single nitrogen from N-Melm. Compound **11** crystallizes in triclinic space group $P_{\bar{1}}$ with a = 13.198 (4) Å, b = 20.294 (6) Å, c = 9.651 (5) Å, α = 90.29 (3)°, β = 98.70 (3)°, γ = 101.54 (2)°, and Z = 2. The dinuclear compound **11** contains one $FeNO_4$ and one FeO_6 coordination sphere in which one N-Melm has been displaced by two solvent DMF molecules. The asymmetric Fe_2O_2 rhombs contain d_{Fe-Fe} of 3.165 (7) Å (**10**) and 3.190 (4) Å (**11**), with Fe-O-Fe angles of 98.9 (3)° (**10**) and 97.7 (5)° and 100.7 (5)° (**11**). Spectroscopic properties of **10** and **11** are compared to those of fully reduced methane monooxygenase (MMO) and the B2 subunit of ribonucleotide reductase (RRB2). The optical spectrum (270-280 nm, 312 nm, ϵ_M = 30000 vs 280-290 nm for MMO), magnetic exchange properties (spin exchange coupling constant $J \approx +2.5$ cm^{-1} vs weak ferromagnetic coupling for MMO), and Mossbauer spectroscopic parameters (δ = 1.18 mm s^{-1}, ΔE_Q = 3.26 mm s^{-1} for **10** and δ_1 = 1.24 mm s^{-1}, ΔE_{Q1} = 3.08 mm s^{-1}, δ_2 = 1.29 mm s^{-1} and ΔE_{Q2} = 2.54 mm s^{-1} for frozen DMF solutions of **10** vs δ = 1.30 mm s^{-1} and ΔE_Q = 3.14 mm s^{-1} for MMO and δ = 1.26 mm s^{-1} and ΔE_Q = 3.13 mm s^{-1} for RRB2) are presented. Cyclic and square-wave voltammetric studies of **11** in DMF revealed two quasi-reversible one-electron oxidation steps at -500 and -250 mV versus SCE corresponding to $[Fe^{2+},Fe^{2+}] \rightarrow [Fe^{2+},Fe^{3+}]$ and $[Fe^{2+},Fe^{3+}] \rightarrow [Fe^{3+},Fe^{3+}]$ core oxidation state transformations. Thus, the mixed-valence species is thermodynamically stable with a comproportionation constant $K_{com} = 1.7 \times 10^4$. A comparison of these results with those reported for MMO (-135 and +48 mV vs NHE) is presented. The proton NMR spectrum of DMSO solutions of **11** is reported as are electron spin resonance studies which reveal integer spin features at $g \approx 12$ (vs $g \approx 16$ for MMO and RRB2) in frozen DMF glasses at 4.2 K.

The chemistry of non-heme iron centers has recently experienced a resurgence of interest owing to their ability to act as alkane/arene oxidation catalysts.[1] Mechanistic investigations of non-heme ferrous oxygenases have suggested the involvement of a $[Fe^{2+}O \leftrightarrow Fe^{4+}{=}O]$ reactive intermediate similar to the ferryl species found in the cytochrome P_{450} pathway. Mononuclear sites of this type are proposed for the tetrahydrobiopterin-dependent hydroxylases,[2] the α-ketoglutarate-dependent hydroxylases,[3] bacterial ω-hydroxylase,[4] isopenicillin-*N* synthase,[5] the aromatic dioxygenases,[6] and in the metalloantibiotic, bleomycin.[7]

More recently, an analogous high-valent FeO^{n+} species was proposed as the key intermediate in the catalytic cycle of soluble methane monooxygenase (MMO) found in methanotrophic bacteria.[8,9] The diiron active site of MMO catalyzes the initial oxidation step in the conversion of methane to CO_2 in which one atom of dioxygen is incorporated into the C-H bond of methane to yield methanol.[10,11] While structurally similar to the dinuclear iron-oxo centers of hemerythrin (HR),[12] ribonucleotide reductase (RR),[13] and the purple acid phosphatases (PAP),[14] this unique site not only catalyzes the conversion of methane to methanol but also the incorporation of an oxygen atom of O_2 into alkanes, alkenes, ethers, and alicyclic, aromatic, and heterocyclic compounds.[10,11]

While only limited structural characterization for representative members of the mononuclear Fe sites found in metalloproteins has been presented,[15,16] the dinuclear Fe site found in MMO has been particularly well-characterized through spectroscopic investigations.[9] The resting diiron(III) core of the hydroxylase component of MMO isolated from the type I methanotroph *Methylococcus capsulatus* (Bath) can be sequentially reduced, generating $[Fe^{3+}, Fe^{3+}]$, $[Fe^{2+}, Fe^{3+}]$, and $[Fe^{2+}, Fe^{2+}]$ centers with midpoint potentials of +48 and -135 mV (vs NHE), respectively.[9f] EXAFS analysis of fully oxidized MMO from *Methylobacterium* CRL-26 is reported to possess four to six oxygen or nitrogen ligands at an average distance of 1.92 Å and a μ-oxo or μ-hydroxo bridge with d_{Fe-Fe} = 3.05 Å.[9b] Recently,

[†] Yale University.
[‡] Massachusetts Institute of Technology.

(1) Hughes, M. N. *Microbial Gas Metabolism, Mechanistic, Metabolic and Biotechnological Aspects*; Poole, R. K., Dow, C. S., Eds.; Academic Press: London, 1985; Chapter 1, p 3.
(2) (a) *Folates and Pterins*; Volume 2, *Chemistry and Bioochemistry of Pterins*; Blakley, R. L., Benkovic, S. J., Eds.; Wiley-Interscience: New York, 1985. (b) Dix, T.; Benkovic, S. J. *Acc. Chem. Res.* **1988**, *21*, 101. (c) Kaufman, S.; Fisher, D. B. *Molecular Mechanisms of Oxygen Activation*; Hayaishi, O., Ed.; Academic Press: New York, 1974; Chapter 8, p 285. (d) Tayeh, M. A.; Marletta, M. A. *J. Biol. Chem.* **1989**, *264*, 19654.
(3) (a) Thornburg, L. D.; Stubbe, J. *J. Am. Chem. Soc.* **1989**, *111*, 7632 and references therein. (b) Britsch, L.; Grisebach, H. *Eur. J. Biochem.* **1986**, *156*, 569. (c) Hashimoto, T.; Yamada, Y. *Eur. J. Biochem.* **1987**, *164*, 277. (d) Lindstedt, G.; Lindstedt, S.; Nordin, I. *Biochemistry* **1977**, *16*, 2181. (e) Abbott, M. J.; Udenfriend, S. *Molecular Mechanisms of Oxygen Activation*; Hayaishi, O., Ed.; Academic Press: New York, 1974; p 168.
(4) McKenna, E. J.; Coon, M. J. *J. Biol. Chem.* **1970**, *245*, 3882.
(5) (a) Robinson, J. A. *Chem. Soc. Rev.* **1988**, *17*, 383 and references therein. (b) Baldwin, J. E.; Abraham, E. *Nat. Prod. Rep.* **1988**, *5*, 129 and references therein.
(6) (a) Batie, C. J.; LaHaie, E.; Ballou, D. P. *J. Biol. Chem.* **1987**, *262*, 1510. Ballou, D.; Batie, C. In *Oxidases and Related Redox Systems*; King, T. E., Mason, H. S., Morrison, M., Eds.; Alan R. Liss, Inc.: New York, 1988, p 211. (b) Axcell, B. C.; Geary, P. J. *Biochem. J.* **1975**, *146*, 173. (c) Ensley, B. D.; Gibson, D. T. *J. Bacteriol.* **1983**, *155*, 505. (d) Yamaguchi, M.; Fujisawa, H. *J. Biol. Chem.* **1982**, *257*, 12497. (e) Subramanian, V.; Liu, T. N.; Yeh, W. K.; Gibson, D. T. *Biochem. Biophys. Res. Commun.* **1979**, *91*, 1131.
(7) (a) Umezawa, H. In *Bleomycin: Chemical, Biochemical and Biological Aspects*; Hecht, S. M., Ed.; Springer-Verlag: New York, 1979. (b) Dabrowiak, J. C. *Adv. Inorg. Biochem.* **1983**, 4 and references therein.
(8) (a) Green, J.; Dalton, H. *J. Biol. Chem.* **1989**, *264*, 17698. (b) Fox, B. G.; Borneman, J. G.; Wackett, L. P.; Lipscomb, J. D. *Biochemistry* **1990**, *29*, 6419.
(9) (a) Woodland, M. P.; Patil, D. S.; Cammack, R.; Dalton, H. *Biochim. Biophys. Acta* **1986**, *873*, 237. (b) Prince, R. C.; George, G. N.; Savas, J. C.; Cramer, S. P.; Patel, R. N. *Biochim. Biophys. Acta* **1988**, *952*, 220. (c) Ericson, A.; Hedman, B.; Hodgson, K. O.; Green, J.; Dalton, H.; Bentsen, J. G.; Beer, R. H.; Lippard, S. J. *J. Am. Chem. Soc.* **1988**, *110*, 2330. (d) Fox, B. G.; Surerus, K. K.; Munck, E.; Lipscomb, J. D. *J. Biol. Chem.* **1988**, *263*, 10553. (e) Hendrich, M. P.; Munck, E.; Fox, B. G.; Lipscomb, J. D. *J. Am. Chem. Soc.* **1990**, *112*, 5861. (f) Liu, K. E.; Lippard, S. J. *J. Biol. Chem.*, in press.

0002-7863/91/1513-8686$02.50/0

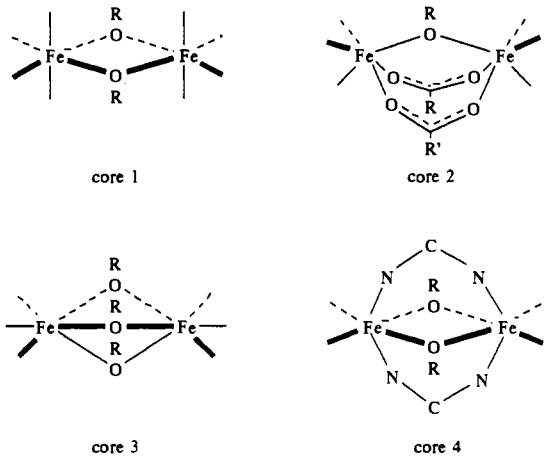

Figure 1. Bridge units observed in crystallographically characterized dinuclear Fe^{2+} complexes. In each case, the remainder of the coordination sphere is composed of either oxygen, nitrogen, or a mixture of these donor atoms.

Mossbauer and integer spin EPR studies performed on MMO purified from *Methylosinus trichosporium* OB3b concluded that the Fe^{2+} centers are weakly ferromagnetically coupled and suggested the presence of either a μ-OH or μ-OR bridge moiety.[9d,e,11] The occurrence of such a structural element in a monooxygenase active site is unique and therefore suggests novel oxygen activation and oxygen atom transfer reactions.

Substantial efforts have been directed toward the synthesis of small molecule analogues of the dinuclear iron active sites found in MMO, hemerythrin, ribonucleotide reductase, and purple acid phosphatase.[17-19] Although significant insight into these dinuclear active sites has derived from spectroscopic studies of stable but nonphysiologically relevant [Fe^{3+}, Fe^{3+}] models containing the μ-oxo/bis(μ-carboxylato) moiety, a detailed understanding of the coordination chemistry, spectroscopic characteristics, and reactivity properties of their fully reduced states has been hindered by the small set of appropriate complexes.[17-19] The [Fe^{2+}, Fe^{2+}] states in MMO and hemerythrin are of particular importance owing to studies strongly suggesting that they are the only core oxidation levels capable of supporting catalytic turnover or dioxygen transport chemistry, respectively.[18]

All structurally characterized dinuclear ferrous model complexes are found to contain one of the four types of core structures shown in Figure 1. Structures containing core unit 1 were reported for complexes using the Robson macrocyclic binucleating ligand,[20] $[Fe_2(Tthd)(A)_4]^{2+}$ (**1**) (A = py, MeNic, MeIm, Im).[21] The most prevalent core structure reported for dinuclear ferrous complexes involves core unit 2, an excellent structural representation for deoxyhemerythrin (R = H). Complexes of the type $[Fe_2(Me_3Tacn)_2(OAc)_2(OH)]^+$ (**2**),[22] $[Fe_2(Bipm)_2(\mu\text{-}\kappa^2O\text{-}O_2CH)_2(\mu\text{-}\kappa O\text{-}O_2CH)(O_2CH)]$ (**3**),[23] $[Fe_2(Bpmp)(O_2CR')_2]^{2+}$ (**4**),[24] and $[Fe_2(N\text{-}Et\text{-}Hptb)(OBz)]^{2+}$ (**5**)[25] are examples of complexes with R = H, aryl, and formyl groups, R' = alkyl or aryl and mixtures thereof. Core unit 3 is reported for the clathrochelate complex, $[Fe_2(Tathip)]^+$ (**6**),[26] which contains encapsulated ferrous centers. Finally, $[Fe_2(Salmp)_2]^{2+}$ (**7**)[27] was observed to have the unique structural elements shown in core unit 4. However, with the exception of complexes **3** and **5**, none of the diferrous compounds have open coordination sites available for dioxygen or substrate binding. Exposure of a solution of **3** to air allowed the isolation of $[Fe_2(Bipm)_2O(\eta^1\text{-}O_2CH)_2(\eta^2\text{-}O_2CH)_2]$ whose μ-oxo bridge originates from molecular oxygen.[23] Recently, the reaction of **5** at −60 °C with dioxygen was reported to lead to a species consistent with the formulation of a peroxo adduct.[25]

The catalytic ability of two dinuclear μ-oxo/bis(μ-carboxylato) ferric compounds has recently been reported. In the presence of molecular oxygen, Zn powder and glacial acetic acid $[Fe_2(HBPz_3)_2O(OAc)_2]$ (**8**)[28a] and $[Fe_2(bipy)_2O(OAc)_2Cl_2]$ (**9**)[28b] were

(10) (a) Colby, J.; Dalton, H. *Biochem. J.* **1976**, *157*, 495. (b) Colby, J.; Stirling, D. I.; Dalton, H. *Biochem. J.* **1977**, *165*, 395. (c) Colby, J.; Dalton, H. *Biochem. J.* **1978**, *171*, 461. (d) Woodland, M. P.; Dalton, H. *J. Biol. Chem.* **1984**, *259*, 53. (e) Lund, J.; Woodland, M. P.; Dalton, H. *Eur. J. Biochem.* **1985**, *147*, 297. (f) Dalton, H.; Leak, D. J. *Gas Enzymology, Proceedings of the Symposium*; Meeting Date 1984, Degn, H., Cox, R. P., Toftlund, H., Eds.; Reidel: Dordrecht, Netherlands, 1985; p 169. (g) Prior, S. D.; Dalton, H. *FEMS Microbiol. Lett.* **1985**, *29*, 105. (h) Dalton, H.; Prior, S. D.; Leak, D. J.; Stanley, S. H. *Microbial Growth C1 Compounds, Proceedings of the International Symposium*; Meeting Date 1983, Crawford, R. L., Hanson, R. S. American Society of Microbiology: Washington, DC 1984; p 75. (i) Leak, D. J.; Stanley, S. H.; Dalton, H. *Spec. Publ. Soc. Gen. Microbiol., 14 (Microb. Gas Metab.)* **1985**, 201. (j) Green, J.; Dalton, H. *Biochem. J.* **1986**, *236*, 155. (k) Leak, D. J.; Dalton, H. *Biocatalysis* **1987**, *1(1)*, 23. (l) Green, J.; Dalton, H. *J. Biol. Chem.* **1988**, *263*, 17561. (m) Green, J.; Dalton, H. *Biochem. J.* **1989**, *259*, 167. (n) Stainthorpe, A. C.; Murrell, J. C.; Salmond, G. P. C.; Dalton, H.; Lees, V. *Arch. Microbiol.* **1989**, *152*, 154. (o) Smith, D. D. S.; Drummond, S.; Dalton, H. *Eur. J. Biochem.* **1989**, *182*, 667.

(11) (a) Fox, B. G.; Lipscomb, J. D. *Biochem. Biophys. Res. Commun.* **1988**, *154*, 165. (b) Fox, B. G.; Froland, W. A.; Dege, J. E.; Lipscomb, J. D. *J. Biol. Chem.* **1989**, *264*, 10023.

(12) (a) Okamura, M. Y.; Klotz, I. M. *Inorg. Biochem.*; Eichhorn, G. L., Ed.; Elsevier: Amsterdam, 1973; p 320. (b) Kurtz, D. M., Jr.; Shriver, D. F.; Klotz, I. M. *Coord. Chem. Rev.* **1977**, *24*, 145.

(13) (a) Lammers, M.; Follmann, H. *Struct. Bonding (Berlin)* **1983**, *54*, 27. (b) Sjoberg, B.-M.; Graslund, A. *Adv. Inorg. Biochem.* **1983**, *5*, 87. (c) Ashley, G. W.; Stubbe, *J. Pharmacol. Ther.* **1987**, *30*, 301. (d) Graslund, A.; Sahlin, M.; Sjoberg, B.-M. *EHP Environ. Health Perspect.* **1985**, *645*, 139. (e) Larsson, A.; Sjoberg, B.-M. *EMBO J.* **1986**, *5*, 2037. (f) Joelson, T.; Uhlin, U.; Eklund, H.; Sjoberg, B.-M.; Hahne, S.; Karlsson, M. *J. Biol. Chem.* **1984**, *259*, 9076. (g) Sjoberg, B.-M.; Loehr, T. M.; Sanders-Lohr, J. *Biochemistry* **1982**, *21*, 96. (h) Petersson, L.; Graslund, A.; Ehrenberg, A.; Sjoberg, B.-M.; Reichard, P. *J. Biol. Chem.* **1980**, *255*, 6706. (i) Atkin, C. L.; Thelander, L.; Reichard, P.; Lang, G. *J. Biol. Chem.* **1973**, *248*, 7464. (j) Nordlund, P.; Sjoberg, B.-M.; Eklund, H. *Nature* **1990**, *345*, 593.

(14) (a) Antanaitis, B. C.; Aisen, P. *Adv. Inorg. Biochem.* **1983**, *5*, 111. (b) Pyrz, J. W.; Sage, J. T.; Debrunner, P. G.; Que, L., Jr. *J. Biol. Chem.* **1986**, *261*, 11015. (c) Averill, B. A.; Davis, J. C.; Burman, S.; Zirino, T.; Sanders-Loehr, J.; Loehr, T. M.; Sage, J. T.; Debrunner, P. G. *J. Am. Chem. Soc.* **1987**, *109*, 3760. (d) Antanaitis, B. C.; Strekas, T.; Aisen, P. *J. Biol. Chem.* **1982**, *257*, 3766. (e) Lauffer, R. B.; Antanaitis, B. C.; Aisen, P.; Que, L., Jr. *J. Biol. Chem.* **1983**, *258*, 14212. (f) Hunt, D. F.; Yates, J. R., III; Shabanowitz, J.; Zhu, N. Z.; Zirino, T.; Averill, B. A.; Daurat-Larroque, S. T.; Shewale, J. G.; Roberts, R. M.; Brew, K. *Biochem. Biophys. Res. Commun.* **1987**, *144*, 1154. (g) Hefler, S. K.; Averill, B. A. *Biochem. Biophys. Res. Commun.* **1987**, *146*, 1173. (h) Kauzlarich, S. M.; Teo, B. K.; Zirino, T.; Burman, S.; Davis, J. C.; Averill, B. A. *Inorg. Chem.* **1986**, *25*, 2781. (i) Vincent, J. B.; Crowder, M. W.; Averill, B. A. *Biochemistry* **1991**, *30*, 3025.

(15) Cox, D. D.; Benkovic, S. J.; Bloom, L. M.; Bradley, F. C.; Nelson, M. J.; Que, L., Jr.; Wallick, D. E. *J. Am. Chem. Soc.* **1988**, *110*, 2026.

(16) Ming, L.-J.; Que, L., Jr.; Kriauciunas, A.; Frolik, C. A.; Chen, V. C. *Inorg. Chem.* **1990**, *29*, 1111.

(17) Kurtz, D. M., Jr. *Chem. Rev.* **1990**, *90*, 585 and references therein.

(18) (a) Lippard, S. J. *Angew. Chem., Int. Ed. Engl.* **1988**, *27*, 344 and references therein. (b) Vincent, J. B.; Olivier-Lilley, G. L.; Averill, B. A. *Chem. Rev.* **1990**, *90*, 1447.

(19) Que, L., Jr.; Scarrow, R. C. *Metal Clusters in Proteins*; Que, L., Jr. Ed.; American Chemical Society Symposium Series No. 372; American Chemical Society: Washington, DC, 1988; Chapter 8, p 152 and references therein.

(20) Abbreviations: Bipm, bis(1-methylimidazol-2-yl)phenylmethoxymethane; bpy, bipyridine; Bpmp, 2,6-bis[bis(2-pyridylmethyl)aminomethyl]-4-methylphenolate(1−); H_4Hbab, 1,2-bis(2-hydroxybenzamido)benzene; $HBpz_3$, tris(pyrazolyl)borate(1−); Hptb, *N,N,N',N'*-tetrakis(2-benzimidazolylmethyl)-2-hydroxy-1,3-diaminopropane; Im, imidazole; Me_3tacn, 1,4,7-trimethyl-1,4,7-triazacyclononane; Salmp, 2-bis(salicylideneamino)methylphenolate(3−); Salpeen, *N,N'*-[2-(2'-pyridyl)ethyl]ethylenebis[salicylideneiminate]; SalRdpt, *N,N'*-(3,3'-dipropylmethylamine)bis(salicylideneiminate); TBAT, tetrabutylammonium tetrafluoroborate; Tpa, tris(2-pyridylmethyl)amine; Tthd, 11,23-dimethyl-3,7,15,19-tetraazatricyclo-[19.3.1.1^{9,13}]hexacosa-2,7,9,11,13(26),14,19,21(25),22,24-decaene-25,26-diol.

(21) Spiro, C. L.; Lambert, S. L.; Smith, T. S.; Duesler, E. N.; Gagne, R. R.; Hendrickson, D. N. *Inorg. Chem.* **1981**, *20*, 1229.

(22) Hartman, J. A. R.; Rardin, R. L.; Chaudhuri, P.; Pohl, K.; Wieghardt, K.; Nuber, B.; Weiss, J.; Papaefthymiou, G. C.; Frankel, R. B.; Lippard, S. J. *J. Am. Chem. Soc.* **1987**, *109*, 7387.

(23) (a) Tolman, W. B.; Bino, A.; Lippard, S. J. *J. Am. Chem. Soc.* **1989**, *111*, 8522. (b) Tolman, W. B.; Liu, S.; Bentsen, J. G.; Lippard, S. J. *J. Am. Chem. Soc.* **1991**, *113*, 152.

(24) (a) Borovik, A. S.; Que, L., Jr. *J. Am. Chem. Soc.* **1988**, *110*, 2345. (b) Borovik, A. S.; Hendrich, M. P.; Holman, T. R.; Munck, E.; Papaefthymiou, V.; Que, L., Jr. *J. Am. Chem. Soc.* **1990**, *112*, 6031.

(25) Menage, S.; Brennan, B. A.; Juarez-Garcia, C.; Munck, E.; Que, L., Jr. *J. Am. Chem. Soc.* **1990**, *112*, 6423.

(26) Timken, M. D.; Marritt, W. A.; Hendrickson, D. N.; Gagne, R. A.; Sinn, E. *Inorg. Chem.* **1985**, *24*, 4202.

(27) Snyder, B. S.; Patterson, G. S.; Abrahamson, A. J.; Holm, R. H. *J. Am. Chem. Soc.* **1989**, *111*, 5214.

observed to catalytically hydroxylate simple organic molecules. While these observations are of significant interest, the nature of the active catalytic species is unknown owing to the instability of these compounds under the reaction conditions. Recently, the spectroscopic characterization of a mononuclear non-heme ferryl species resulting from peroxide-induced fragmentation of a diferric complex $[Fe_2O(Tpa)_2]^{2+}$ was reported.[29]

In connection with our interest in biological Fe^{2+} based oxygen atom transfer chemistry, we have developed an analogue reaction system for dinuclear ferrous centers that can catalyze the transfer of an oxygen atom from PhIO to a variety of simple organic substrates.[30] As a consequence of the $[Fe{=}O]^{n+}$ species proposed in the MMO mechanism, we have utilized simple diamide chelating ligands which have a demonstrated ability to stabilize high formal transition-metal oxidation states[31] with the expressed purpose of examining the atom transfer properties of such complexes. The use of the ligand 1,2-bis(2-hydroxybenzamido)benzene (H_4Hbab) allows the formation of $[Fe_2(H_2Hbab)_2(N\text{-MeIm})_2]$ (**10**) and its DMF solvate $[Fe_2(H_2Hbab)_2(DMF)_2(N\text{-MeIm})]$

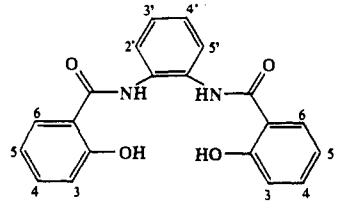

Ligand Numbering Scheme

(**11**). In addition to the catalytic atom transfer capability of **11**,[30] both **10** and **11** exhibit electronic properties closely related to the fully reduced cores of soluble MMO and RRB2. Presented for the first time here are the full details of the crystal structure determinations of **10** and **11** and measurements of their UV–vis, infrared, electrochemical, ^{1}H NMR, EPR, Mossbauer, and magnetic properties along with comparisons to the spectroscopically characterized cores of MMO and RRB2.

Experimental Section

Methods and Materials. The diamide ligand H_4Hbab[20] and its dilithium salt were prepared by published methods.[30,31] Analogous procedures using 3-, 4-, and 5-(methylacetyl)salicylic acids and 4,5-dimethyl-1,2-phenylenediamine were employed in the synthesis of methyl-substituted derivatives of H_4Hbab required for NMR signal assignments of Fe complexes.[32] All other reagents were purchased from commercial sources and purified by standard methods. Solvents were appropriately purified, dried, and degassed prior to use.

$Fe_2(H_2Hbab)_2(N\text{-MeIm})_2\cdot MeOH$ (10). All operations were carried out under a dinitrogen atmosphere. To a stirred solution of 2.0 g (5.5 mmol) of *trans*-$Fe(N\text{-MeIm})_2(Cl)_2(MeOH)_2$[33] in 40 mL of methanol was added a filtered solution of 2.0 g (5.5 mmol) of Li_2H_2Hbab in 50 mL of methanol. The pale yellow solution of *trans*-$Fe(N\text{-MeIm})_2(Cl)_2(MeOH)_2$ turned a deeper yellow color upon addition of the Li_2H_2Hbab solution. After 5–15 min of stirring, a bright yellow microcrystalline precipitate began to appear. The resulting suspension was stirred overnight at ambient temperatures and then filtered to give 4.0 g (71%) of the pure product soluble in DMF and DMSO and insoluble in most common organic solvents [Anal. Calcd for $C_{49}H_{44}Fe_2N_8O_9$: C, 58.80; H, 4.43; Fe, 11.18; N, 11.20. Found: C, 59.34; H, 4.16; Fe, 10.80; N, 11.50. Absorption spectrum (CH_2Cl_2/1% DMF) λ_{max} (ϵ_M) 312 (sh, 30000) nm. Infrared spectrum (KBr) $\nu_{amideNH}$ = 3450 cm^{-1}, $\nu_{amideCO}$ = 1640 cm^{-1}]. This compound is oxygen-sensitive as a solid and extremely so in solution; it forms bright yellow solutions.

Table I. Crystallographic data for $[Fe_2(H_2Hbab)_2(N\text{-MeIm})_2]$, **10**, and $[Fe_2(H_2hbab)_2(N\text{-MeIm})(DMF)_2]\cdot DMF$, **11**

	10	**11**
formula	$C_{24}H_{20}O_4N_4Fe$	$C_{50}H_{48}O_{10}N_8Fe_2$
formula wt, amu	484.29	1032.67
temp, K	296	296
crystal system	triclinic	triclinic
space group	$P\bar{1}$ (no. 2)	$P\bar{1}$ (no. 2)
a, Å	9.969 (4)	13.198 (4)
b, Å	12.754 (5)	20.294 (6)
c, Å	9.919 (7)	9.651 (5)
α	100.60 (5)	90.29 (3)
β	118.40 (4)	98.70 (3)
γ	77.42 (3)	101.54 (3)
V, Å^3	1078 (1)	2052 (2)
Z	2	2
ρ_{calcd}, g cm^{-3}	1.492	1.371
crystal dim, mm	0.25 × 0.23 × 0.15	0.20 × 0.18 × 0.15
radiation	Cu Kα (λ = 1.54178 Å)	Cu Kα (λ = 1.54178 Å)
μ, cm^{-1}	59.55	51.92
scan type	ω	ω
2θ range, deg	≤114	≤114
reflctns	3114	7137
	1424$I \geq 3\sigma(I)$	2693$I \geq 3\sigma(I)$
no. least-sq param	298	654
reflctn/params	4.78	4.12
$R(F_o)$	6.4%	7.8%
$R_w(F_o)$	6.6%	7.9%
GOF	1.77	1.48
p-factor	0.03	0.03

Collection and Reduction of X-ray Data. $Fe_2(H_2Hbab)_2(N\text{-MeIm})_2$ (10) and $Fe_2(H_2Hbab)_2(N\text{-MeIm})(DMF)_2$ (11). Single crystals of **10** were obtained from a saturated MeOH solution (≈1 mM) over a period of 15 days, while crystals of **11** were obtained by the slow diffusion of ether into a 0.025 M solution of **10** in DMF over a period of 18 days at ambient temperature in an inert atmosphere box. A light orange parallelpiped-shaped crystal of **10** and an irregularly shaped dark brown crystal of **11** were mounted in a random orientation in glass capillaries under an inert atmosphere. Data collection was carried out at ambient temperature on a four-cycle Rigaku AFC5S fully automated diffractometer using graphite-monochromated Cu Kα radiation. The unit cell parameters were obtained from a least-squares refinement using the setting angles of 18 (**10**) and 15 (**11**) carefully centered reflections in the range 19° ≤ 2θ ≤ 33° which corresponded to a triclinic cell. Intensities of three check reflections (−1,1,−1; −2,1,0; −3,1,1 for **10** and 1,4,0; 2,2,1; 2,2,−1 for **11**) measured every 150 reflections indicated no significant decay in intensities over the course of data collection. Data sets were processed using SHELX586 and the WFOUR option in DIRDIF. All calculations were performed using the TEXSAN crystallographic software package (Molecular Structure Corporation, The Woodlands, TX, 77381). Empirical absorption corrections, applied using the program DIFABS, resulted in transmission factors ranging from 0.75 to 1.00 for **10** and from 0.82 to 1.42 for **11**. Crystallographic data for **10** and **11** are summarized in Table I.

Structure Solution and Refinement. Atom scattering factors were taken from a standard source.[35] Both space groups were determined to be $P\bar{1}$ (No. 2), Z = 2. The structure of **10** was solved using the position of the Fe atom from the Patterson function and DIRDIF where the entire structure was located on a difference Fourier map. For **11**, the Fe atoms and fragments of the ligands were visible in the initial electron density map computed using SHELX586. The remainder of the structure was elucidated using the WFOUR option in DIRDIF. All hydrogens were calculated and assigned isotropic thermal parameters which were 20% greater than the equivalent value of the atom to which they were bonded. They were included in the refinement with their structure factor contributions but otherwise not refined. The refinement of **10**, based on 1424

(28) (a) Kitajima, N.; Fukui, H.; Moro-oka, Y. *J. Chem. Soc., Chem. Commun.* **1988**, 485. (b) Vincent, J. B.; Huffman, J. C.; Christou, G.; Li, Q.; Nanny, M. A.; Hendrickson, D. N.; Fong, R. H.; Fish, R. H. *J. Am. Chem. Soc.* **1988**, *110*, 6898.

(29) Leising, R. A.; Brennan, B. A.; Que, L., Jr.; Fox, B. F.; Munck, E. *J. Am. Chem. Soc.* **1991**, *113*, 3988.

(30) Stassinopoulos, A.; Caradonna, J. P. *J. Am. Chem. Soc.* **1990**, *112*, 7071.

(31) (a) Anson, F. C.; Christie, J. A.; Collins, T. J.; Coots, R. J.; Furutani, T. T.; Gipson, S. L.; Keech, J. T.; Krafft, T. E.; Santarsiero, B. D.; Spies, G. H. *J. Am. Chem. Soc.* **1984**, *106*, 4460. (b) Collins, T. J.; Coots, R. J.; Furutani, T. T.; Keech, J. T.; Peake, G. T.; Santarsiero, B. D. *J. Am. Chem. Soc.* **1986**, *108*, 5333. (c) Anson, F. C.; Collins, T. J.; Gipson, S. L.; Keech, J. T.; Krafft, T. E.; Peake, G. T. *J. Am. Chem. Soc.* **1986**, *108*, 6593.

(32) Stassinopoulos, A.; Caradonna, J. P, manuscript in preparation.

(33) *trans*-$Fe[(N\text{-MeIm})_2(Cl)_2(MeOH)_2]$ was prepared by a modification of a literature procedure.[34] A stoichiometric amount of a 50% MeOH/N-MeIm solution (7.6 mL) was rapidly added under an inert atmosphere to a solution of 3.0 of $FeCl_2$ in 50 mL of MeOH. Upon standing overnight a white precipitate was observed. The solvent volume was reduced to ≈10 mL, and the microcrystalline material was filtered to give 6.3 g of product (74.5% yield). Stassinopoulos, A.; Schulte, G.; Papaefthymiou, G. C.; Caradonna, J. P., manuscript in preparation.

(34) Long, G. J.; Whitney, D. L.; Kennedy, J. E. *Inorg. Chem.* **1971**, *10*, 1406.

(35) Cromer, D. T.; Waber, J. T. *International Tables for X-ray Crystallography*; Kynoch Press: Birmingham, England, 1974.

Table II. Selected Interatomic Distances (Å) and Angles (deg) in $[Fe_2(H_2Hbab)_2(N\text{-MeIm})_2]$, **10**, and $[Fe_2(H_2Hbab)_2(DMF)_2(N\text{-MeIm})]\cdot DMF$, **11**

Compound **10**

Fe–O(1)	1.948 (7)	O(1)–Fe–O(3)	91.0 (3)
Fe–O(3)	2.150 (7)	O(1)–Fe–O(4)	117.0 (3)
Fe–O(4)	1.997 (7)	O(1)–Fe–O(4)′	98.6 (3)
Fe–O(4)′	2.167 (7)	O(1)–Fe–N(3)	127.6 (3)
Fe–N(3)	2.080 (9)	O(3)–Fe–O(4)	84.6 (3)
		O(3)–Fe–O(4)′	165.3 (3)
		O(3)–Fe–N(3)	89.4 (3)
O(4)–O(4)′		O(4)–Fe–N(3)	115.2 (3)
Fe–Fe′	3.165 (7)	O(4)′–Fe–N(3)	93.5 (3)
		O(4)–Fe–O(4)′	81.1 (3)
		Fe(1)–O(4)–Fe′	98.9 (3)

Compound **11**

Fe(1)		Fe(2)	
Fe(1)–O(1)	1.91 (1)	Fe(2)–O(4)	2.22 (1)
Fe(1)–O(3)	2.12 (1)	Fe(2)–O(5)	1.99 (1)
Fe(1)–O(4)	2.01 (1)	Fe(2)–O(7)	2.16 (1)
Fe(1)–O(8)	2.08 (1)	Fe(2)–O(8)	2.06 (1)
Fe(1)–N(3)	2.03 (2)	Fe(2)–O(9)	2.16 (1)
O(4)–O(8)	2.70 (2)	Fe(2)–O(10)	2.12 (1)
Fe(1)–Fe(2)	3.190 (4)		
O(1)–Fe(1)–O(3)	85.3 (4)	O(4)–Fe(2)–O(5)	101.2 (5)
O(1)–Fe(1)–O(4)	124.1 (5)	O(4)–Fe(2)–O(7)	162.9 (4)
O(1)–Fe(1)–O(8)	103.1 (5)	O(4)–Fe(2)–O(8)	78.1 (4)
O(1)–Fe(1)–N(3)	124.2 (6)	O(4)–Fe(2)–O(9)	104.9 (5)
O(3)–Fe(1)–O(4)	85.6 (4)	O(4)–Fe(2)–O(10)	88.5 (4)
O(3)–Fe(1)–O(8)	168.1 (5)	O(5)–Fe(2)–O(7)	84.8 (5)
O(3)–Fe(1)–N(3)	87.2 (6)	O(5)–Fe(2)–O(8)	96.3 (5)
O(4)–Fe(1)–O(8)	82.7 (4)	O(5)–Fe(2)–O(9)	88.1 (5)
O(4)–Fe(1)–N(3)	110.2 (6)	O(5)–Fe(2)–O(10)	168.4 (5)
O(8)–Fe(1)–N(3)	94.8 (5)	O(7)–Fe(2)–O(8)	85.3 (4)
		O(7)–Fe(2)–O(9)	91.2 (5)
Fe(1)–O(4)–Fe(2)	97.7 (5)	O(7)–Fe(2)–O(10)	87.7 (5)
Fe(1)–O(8)–Fe(2)	100.7 (5)	O(8)–Fe(2)–O(9)	174.0 (6)
		O(8)–Fe(2)–O(10)	91.9 (5)
		O(9)–Fe(2)–O(10)	83.1 (5)

observed reflections (49%) with $I \geq 3\sigma(I)$, converged with $R = 6.4\%$ and $R_w = 6.6\%$, while the refinement of **11**, based on 2693 observed reflections $I \geq 3\sigma(I)$ and 654 variable parameters, converged with the following conventional crystallographic values: $R = 7.8\%$ and $R_w = 7.9\%$. In **11**, one lattice DMF solvent molecule was found to have partial occupancy and to be disordered. Owing to data limitations, this disorder was not modeled. Selected bond lengths and angles for **10** and **11** are reported in Table II. A complete listing of the fractional coordinates, temperature factors, bond distances, torsional angles, anisotropic temperature factors, and stereoscopic view of the unit cells have been deposited as supplementary material.

Physical Methods. All measurements were performed under strictly anaerobic conditions. The solution molecular weight determination was performed using the Signer method.[36] The standard solution (1.0 mL) was 2×10^{-5} M PPh_3 in MeOH, while the solution (1.0 mL) of **10** was 1.33×10^{-4} M in Fe. The apparatus was sealed and maintained at ambient temperature. Volume measurements were recorded every 24 h for 21 days. UV-vis spectra were recorded at the start and end of the experiment verifying that no oxidation or decomposition had occurred. Electronic absorption spectra were measured on a Perkin-Elmer Lambda 4C spectrophotometer in the 280–900 nm range, while infrared spectra were collected on a Nicolet 5SX FT-IR spectrometer. ^1H NMR spectra were recorded on either a Bruker WM-250 or AM-500 MHz spectrometer operating at ambient temperatures. All shifts are reported vs internal Me_4Si standard. Samples with concentrations of approximately 30 mM required 1024 scans to obtain adequate signal-to-noise ratios. For T_1 measurements, $\tau_{FID} + \tau_{delay}$ was set to 500 ms to ensure complete relaxation of the paramagnetically shifted resonances. The spectra were obtained with the inversion-recovery pulse sequence $(\tau_{delay}-\pi-\tau-\pi/2-\tau_{FID})_n$ using quadrupole phase cycling.[37] A linear baseline correction was applied to the spectrum from which peak positions, widths, and amplitudes were determined. Peak intensities were fit by a nonlinear least-squares program to the equation $I(\tau) = I_\infty[C_1 - C_2\exp(-\tau/T_1)]$ where the parameters T_1, C_1, and C_2 were allowed to vary. The parameters C_1 and C_2 were observed to refine to their expected values indicating proper pulse durations. Scalar J coupling determinations were obtained from a series of two-dimensional homonuclear Hartmann-Hahn (HOHAHA) experiments using the MLEV17 mixing sequence on 50 mM solutions of **10** in DMSO-d_6 on a Bruker AM 500 Spectrometer at 303 K.[38,39] The spectrum results from a $512 \times 1K$ data matrix; zero-filling was used to yield a final $1K \times 1K$ matrix. An acquisition time of 11.3 ms was used. Thirty-two scans were recorded for every value of t_1. The mixing-time consisted of two MLEV-17 cycles, corresponding to a spin-lock time of 5 ms, plus two trim pulses of 0.5 ms each. Off-line data processing was performed on a VAX 1170 using the software package FTNMR.[40] Gaussian broadening was used in both dimensions to minimize truncation errors. Magnetic susceptibility measurements of solids were performed at an applied field of 5 kOe on a SHE SQUID magnetometer operating between 12 and 300 K. Measurements of the magnetic moment at 7 K as a function of field between 1 and 10 kOe demonstrated the lack of saturation effects. Determinations were made on finely ground polycrystalline samples loaded into precalibrated containers and sealed with epoxy resin under a helium atmosphere. Diamagnetic susceptibility corrections, using Li_2H_2Hbab in precalibrated containers, were made. The theoretical expression (vide infra) was fit to the data by a nonlinear least-squares method by using a locally written program on a MacII CX with a floating chip accelerator. Solution susceptibility measurements were performed by the usual NMR method using mesitylene as the standard; solvent susceptibilities were literature values.[41] Cyclic voltammetry electrochemical experiments were carried out with a standard Bioanalytical system (CV-27 Voltamogrpah, C-1A Cell stand, BAS-RXY Recorder) with the use of a Pt working electrode, a Ag wire reference electrode, and 0.1 M tetra-*n*-butylammonium tetrafluoroborate (TBAT) as supporting electrolyte and were conducted at room temperature in an inert atmosphere box. The Fe(0/+) couple of ferrocene (E° = 0.400 V vs NHE) was used as internal standard.[42] Square wave voltammetry experiments were performed with a Princeton Applied Research (PAR) Potentiostat/Galvanostat Model 273 potentiostat and a PAR Model RE0091 X-Y recorder using a platinum electrode.[43] Temperature-dependent EPR spectra were recorded on a JEOL ME-3X X-band EPR spectrometer equipped with an Oxford ESR-900 liquid helium cryostat. Sample temperatures were determined with a carbon-glass resistor (Lake Shore Cryotronics) contained in a sample tube in the sample position.[44] Mossbauer spectra were recorded at 4.2 and 80 K with a conventional constant acceleration spectrometer equipped with a temperature controller, maintaining temperatures within ±0.1 K. The source used was ^{57}Co in Rh, and the isomer shifts were referenced to metallic iron at room temperature.

Results and Discussion

Synthesis. We are continuing to investigate the role of non-heme Fe^{2+} centers in metalloproteins, particularly those centers involved in oxygen atom transfer reactions which are proposed to utilize a $[Fe^{2+}O \leftrightarrow Fe^{4+}{=}O]$ reactive intermediate. To model the reaction chemistry of the diferrous center found in methane monooxygenase, we have found that the reaction of 1 equiv of Li_2H_2Hbab with 1 equiv of *trans*-$Fe(N\text{-MeIm})_2(Cl)_2(MeOH)_2$ in MeOH permits the isolation in 71% yield of a bright yellow product (**10**) which has the stoichiometric formulation $[Fe(H_2Hbab)(N\text{-MeIm})]_n$. The nuclearity of **10** in MeOH was

$$n\text{Li}_2\text{H}_2\text{Hbab} + n\text{trans-Fe(N-MeIm)}_2\text{(Cl)}_2\text{(MeOH)}_2 \rightarrow \text{Fe}_n\text{(H}_2\text{Hbab)}_n\text{(N-MeIm)}_n + 2n\text{LiCl} + n\text{N-MeIm} \quad (1)$$

confirmed by anaerobic isothermal distillation techniques which gave a solution molecular weight of 1000 ± 50 which is consistent only with a dinuclear complex (eq 1, $n = 2$, MW = 968; supplementary material Table S1).[36] No detectable decomposition/oxidation of **10** was observed during the solvent equilibration

(36) (a) Clark, E. P. *Ind. Eng. Chem. Anal. Ed.* **1941**, *13*, 820. (b) Signer, R. *Ann.* **1930**, *478*, 246.
(37) Levy, G. C.; Peat, I. R. *J. Magn. Reson.* **1975**, *18*, 500.
(38) Bax, A.; Davis, D. G. *J. Magn. Reson.* **1985**, *65*, 355.
(39) Braunschweiler, L.; Ernst, R. R. *J. Magn. Reson.* **1983**, *53*, 521.
(40) FTNMR is a program licensed from Hare Research Inc., Woodinville, WA.
(41) (a) Live, D. H.; Chan, S. I. *Anal. Chem.* **1970**, *42*, 791. (b) Wayer, M.; Gerger, U.; Gutmann, V. *Monatsh. Chem.* **1977**, *108*, 489.
(42) Gagne, R. R.; Koval, C. A.; Lisensky, G. C. *Inorg. Chem.* **1980**, *19*, 2855.
(43) (a) Christe, J. H.; Turner, J. A.; Osteryoung, R. A. *Anal. Chem.* **1977**, *49*, 1899. (b) Turner, J. A.; Christie, J. H.; Vukovic, M.; Osteryoung, R. A. *Anal. Chem.* **1977**, *49*, 1904. (c) O'Dea, J. J.; Osteryoung, J.; Osteryoung, R. A. *Anal. Chem.* **1981**, *53*, 695.
(44) Beck, W.; Brudvig, G. *J. Magn. Reson.* **1991**, 90.

Scheme I

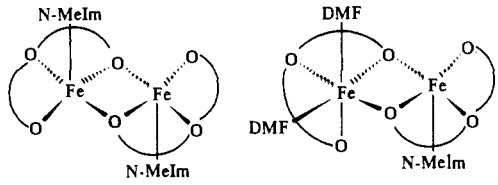

10 11

period (21 days). This product afforded satisfactory elemental analysis after vacuum drying. $Fe_2(H_2Hbab)_2(N\text{-}MeIm)_2$ is practically insoluble in most common solvents (≤0.5 mM) but is quite soluble in DMF and DMSO.

In order to facilitate the assignment of the NMR spectrum, several methyl-substituted derivatives of Li_2H_2Hbab were required. These methylated ligands were synthesized by procedures entirely analogous to that of Li_2H_2Hbab using either 3-, 4-, or 5-(methylacetyl)salicylic acids, 4,5-dimethyl-1,2-phenylenediammine, or combinations thereof.[32] Reaction with *trans*-$Fe(N\text{-}MeIm)_2(Cl)_2(MeOH)_2$ afforded the dinuclear Fe^{2+} complexes in 60–80% yields.

Solid-State Structures of $[Fe_2(H_2Hbab)_2(N\text{-}MeIm)_2]$, 10, and $[Fe_2(H_2Hbab)_2(N\text{-}MeIm)(DMF)_2]$, 11. While the H_2Hbab^{2-} ligand is capable of forming both mononuclear and dinuclear metal complexes, our synthetic scheme exclusively generated dinuclear complexes in high yields. X-ray structure determinations performed on crystals obtained from MeOH solutions (**10**) clearly show two trigonal-bipyramidal Fe atoms sharing a common axial–equatorial edge. The structure of **10**, illustrated schematically in Scheme I and more explicitly in Figure 2a, shows two iron centers bridged by two H_2Hbab^{2-} ligands. Each Fe^{2+} atom is bridged by two phenolate oxygen atoms of different H_2Hbab^{2-} ligands. While this doubly bridged core structure is well-documented for Fe^{3+} centers, reports of its occurrence in structurally characterized dinuclear Fe^{2+} complexes are limited to $[Fe_2(Tthd)(Im)_4]^{2+}$ and $[Fe_2(Salmp)_2]^{2-}$.[21,27] In addition to the bridging phenolate oxygen atoms, each Fe center in **10** is coordinated to an amide oxygen, an additional phenolate oxygen atom and a single N-MeIm giving five-coordinate NO_4 ligand donor sets. The two Fe centers are related by a crystallographically imposed center of symmetry.

X-ray structure determinations performed on crystals of **11** obtained from DMF/Et_2O reveal an asymmetric molecule resulting from the displacement of one N-MeIm molecule in **10** by two solvent DMF molecules. Shown schematically in Scheme I and in Figure 2b, the arrangement of the two H_2Hbab^{2-} ligands in **11** are analogous to that observed for **10**. However, while the coordination sphere for Fe(1) in **11** is completed by a single N-MeIm giving a five-coordinate NO_4 ligand donor set similar to that found in **10**, Fe(2) is bound to two DMF molecules, generating a six-coordinate all oxygen ligand donor sphere.

Analysis of the Fe coordination spheres in **10** and Fe(1) in **11** using the conformational analysis methods of Auf der Heyde and Burgi indicates that each adopts a trigonal-bipyramidal geometry (Figure 3).[45] The atoms O(1), O(4), and N(3) form the equatorial planes with the iron atom being displaced 0.05 Å from the plane toward the bridging phenolate O4′ in **10** and 0.14 Å from the plane toward the bridging phenolate O(8) atom in **11**. The bond angles in the equatorial planes of **10** and **11** are as expected with the exception of N(3)–Fe(1)–O(4) angle of **11** (110.2 (6)°). This is a consequence of the six-membered chelate ring formed from the phenolate O(4) and amide O(3) atoms which span equatorial and axial sites in the trigonal bipyramid. The effect of the chelate ring is also observed in the axial bond angles which deviate by 12–15° from their idealized value. In centrosymmetric **10**, the O(4)′–Fe(1)–O(4) angle is smaller than O(4)′–Fe(1)–N(3), indicating that the Fe(1)–O(4)′ bond is tilted with respect to the equatorial plane in the direction of the O(4) atom. Variations in the angles O(3)–Fe(1)–N(3) > O(3)–Fe(1)–O(1) >

(45) (a) Auf der Heyde, T. P. E.; Burgi, H.-B. *Inorg. Chem.* **1989**, *28*, 3960. (b) Auf der Heyde, T. P. E.; Burgi, H.-B. *Inorg. Chem.* **1989**, *28*, 3970. (c) Auf der Heyde, T. P. E.; Burgi, H.-B. *Inorg. Chem.* **1989**, *28*, 3982.

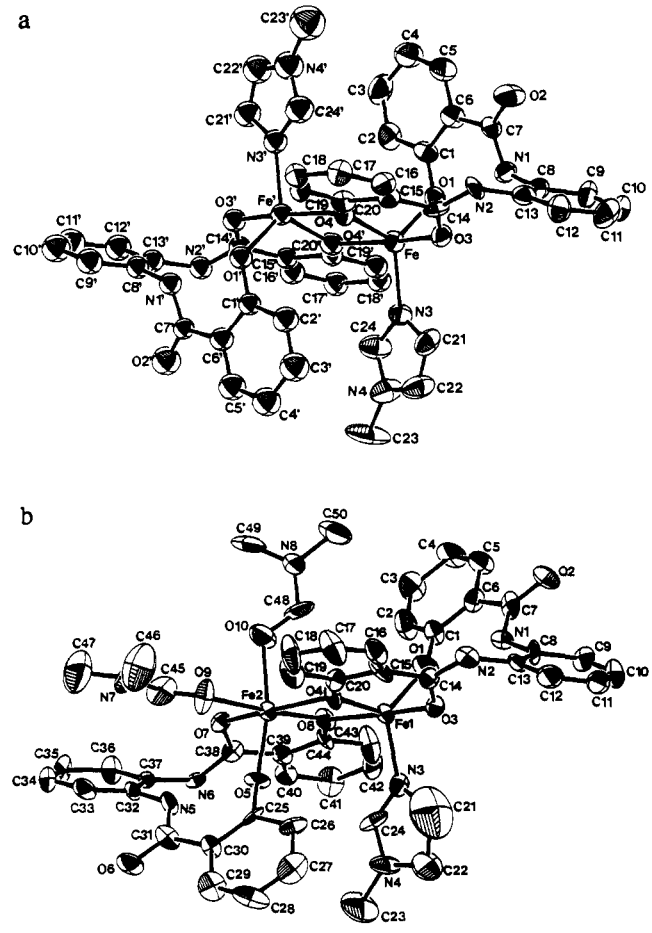

Figure 2. (a) Structure of $[Fe_2(H_2Hbab)_2(N\text{-}MeIm)_2]$, **10**, and (b) $[Fe_2(H_2Hbab)_2(DMF)_2(N\text{-}MeIm)]\cdot DMF$, **11**, showing the 50% probability thermal ellipsoids and atom labeling scheme. The hydrogen atoms are omitted for clarity.

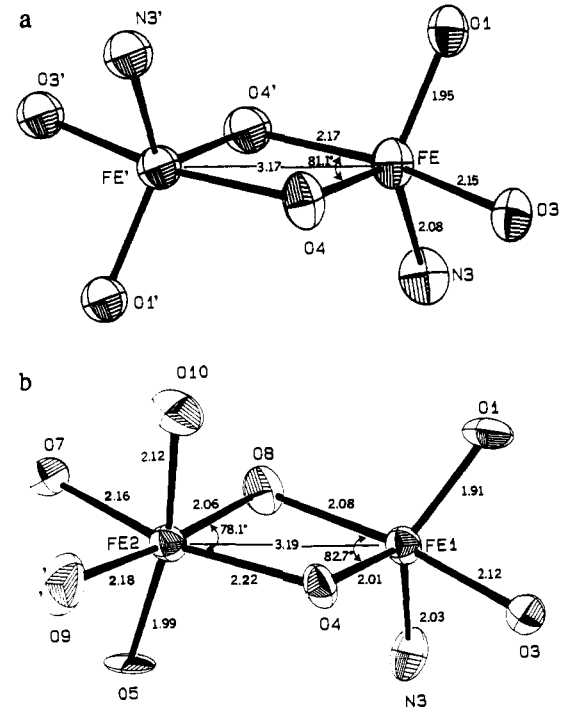

Figure 3. (a) Structure of the coordination spheres of $[Fe_2(H_2Hbab)_2(N\text{-}MeIm)_2]$, **10**, and (b) $[Fe_2(H_2Hbab)_2(DMF)_2(N\text{-}MeIm)]\cdot DMF$, **11**, showing 50% probability thermal ellipsoids and atom labling scheme.

Scheme II

Idealized Fe-Fe distance for core units with $d_{Fe\text{-}O_{equatorial}} = r$, $d_{Fe\text{-}O_{axial}} = 1.1r$

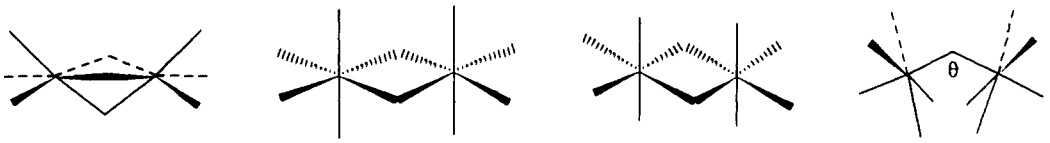

face sharing 1.31r < equatorial edge sharing 1.42r ≤ axial-equatorial edge sharing 1.49r ≤ vertex sharing (2 - 2cosθ)r

O(3)–Fe(1)–O(1) are consistent with a tilt of the axis toward O(4). An entirely analogous trend is observed for Fe(1) in **11**, indicating that the Fe(1)–O(8) bond is tilted with respect to the equatorial plane in the direction of the O(4) atom. This distribution of bond angles is clearly the result of the chelating nature of the ligand and the presence of the bridging phenolate oxygen atoms which significantly affect the details of the coordination sphere about Fe(1).

In each of the five-coordinate centers in **10** and **11**, the $Fe–O_{axial}$ bonds are longer than the $Fe–O_{equatorial}$ bonds. These results parallel those reported for the high-spin trigonal-bipyramidal complexes $[Fe_2(Bmpd)_2]$ and $[Fe(Me_6Tren)Br]^+$.[24,46] The tight binding of the anionic terminal phenolate oxygen atoms is evident by a comparison of the observed $Fe(1)–O_{phenolate}$ bond lengths with other structurally characterized Fe^{2+} systems. The $Fe(1)–O(1)_{equatorial}$ bond distance in either **10** or **11** is somewhat shorter than other reported Fe^{2+}-terminal–phenolate bond lengths observed in dinuclear $[Fe_2(Salmp)_2]^{2-}$, **7** (2.06 Å),[27] and mononuclear Fe^{2+} complexes with either distorted trigonal-bipyramidal geometries ($[Fe^{2+}(Salpeen)]$, 1.96 Å;[47] $[Fe^{2+}(SalRdpt)]$, 1.95 Å[48]) or distorted square-pyramidal geometries ($[Fe^{2+}(5\text{-}NO_2Salen)(S\text{-}p\text{-}tol)]^-$, 2.00 Å[49]). Finally, the effect of bridging vs monodentate phenolate coordination to Fe^{2+} is observed in the bond length difference of 0.05–0.10 Å for equatorial Fe(1)–O(4) and Fe(1)–O(1), respectively.

The arrangement of oxygen atoms about Fe(2) in **11** is best described by a distorted octahedral coordination (Figure 3). The atoms O(5), O(8), O(9), and O(10) form the equatorial plane with the Fe being displaced 0.11 Å below the best plane toward the axial O(4) bridging phenolate oxygen atom. While the equatorial O–Fe(2)–O′ bond angles are within normal ranges, the O(4)–Fe(2)–O(7) angle is significantly distorted from the expected value of 180°. The O(9)–Fe(2)–O(10) angle between two coordinated DMF molecules is a consequence of steric interactions between the bound DMF molecules and the H_2Hbab^{2-} ligand which is wrapping around the metal center while the O(5)–Fe(2)–O(8) angle reflects the chelate role of the O(8),O(7) chelate ring and the bridging nature of O(8). A tilt of the Fe(2)–O(4) bond with respect to the equatorial plane in the direction of O(8) is observed from the O(4)–Fe(2)–O(8) and O(4)–Fe(2)–O(1) angles.

Finally, the axial Fe(2)–O(7) and Fe(2)–O(4) bond lengths are longer than the mean Fe(2)–O equatorial bond lengths. As expected from the higher coordination number, bonds to Fe(2) are longer than analogous bonds to Fe(1) by 0.04 ($Fe(2)–O(7)_{amide}$ vs $Fe(1)–O(3)_{amide}$) to 0.14 Å ($Fe(2)–O(4)_{bridging\ phenolate}$ vs $Fe(1)–O(8)_{bridging\ phenolate}$). The bond lengths for the coordinated DMF molecules are unexceptional.

In the ligand arrangement encountered in **10** and **11**, the two Fe coordination spheres share a common edge involving equatorial and axial phenolate oxygen atoms. The axes of the coordination spheres are parallel as shown in Figure 2. In centrosymmetric **10**, the Fe_2O_2 core is a planar rhomb with significantly unequal Fe–O distances (0.17 Å) and acute O–Fe–O (81.1 (3)°) and obtuse (98.9 (3)°) angles. The nearly planar Fe_2O_2 bridge unit of **11** (interplanar angle between Fe(1)–O(4)–Fe(2) and Fe(1)–O(8)–Fe(2) = −6.7 (5)°) resembles an asymmetric rhomb composed of unequal Fe–O distances and acute O–Fe–O (78–83°) and obtuse Fe–O–Fe (97–102°) angles. Although the coordination of two ligands about the trigonal-bipyramidal and octahedral Fe^{2+} centers in **10** and **11** causes dramatic variations in Fe–O bond lengths (1.91–2.22 Å), these values are within the range reported for other dinuclear ferrous complexes containing bound phenolate anions.[21,23,24,27] The bridging phenolate rings are crystallographically constrained to be parallel in **10** and are nearly so in **11** (5.7°). In both structures, the planes of the phenolate rings are nearly parallel to the Fe–Fe vector (8.9° in **10**, 2–4° in **11**). This is in contrast to the core reported for $[Fe_2(Salmp)_2]^{2+}$ in which the two bridging phenolate rings are at an interplanar angle of 178° to each other and at angles of 86.8° and 94.1° to the Fe–Fe vector.[27] The Fe–Fe distances (3.165 (7) Å for **10**, 3.190 (3) Å for **11**) are considered too long for metal–metal bonding, and the O(4)–O(4)′/O(8) nonbonded distances are 2.71 (3) and 2.70 (2) Å, respectively.

The topology of the H_2Hbab^{2-} ligand shows considerable distortion from its expected planar nature observed in other complexes containing this ligand. While the torsion angle defined by O(2)–C(7)–C(6)–C(5) (**10**, 10 (2)°; **11**, −4 (3)°) shows minor deviations from planarity, a more pronounced effect is observed for C(7)–N(1)–C(8)–C(9) (**10**, −99 (1)°; **11**, −46 (3)°), C(14)–N(2)–C(13)–C(12) (**10**, 128 (1)°; **11**, 125 (3)°) and O(3)–C(14)–C(15)–C(20) (**10**, −23 (2)°; **11**, −20 (3)°) for the ligand about Fe(1). The analogous torsion angles about the six-coordinate Fe(2) center are of comparable magnitude. We are unable to assess the issue of nonplanarity of the amide bonds observed in other complexes containing the H_2Hbab^{2-} ligand owing to limitations of the crystallographic data which preclude identification of the amide proton positions.

There are several unique features of **10** and **11** which become evident upon comparison of their structure with the crystallographically characterized Fe^{2+} complexes containing bridging units 1–4 (Table III). The series of Fe···Fe distances, which follows the trend $[Fe_2(Bipm)_2(O_2CH)_4]$ (**3**, vertex sharing)[23] > $[Fe_2(N\text{-}Et\text{-}Hptb)(OBz)]^{2+}$ (**5**, vertex sharing)[25] > $[Fe_2(Bpmp)(O_2CR')_2]^{2+}$ (**4**, vertex sharing)[24] > $[Fe_2(Me_3tacn)_2(OAc)_2(OH)]^+$ (**2**, vertex sharing)[22] > $[Fe_2(Salmp)_2]^{2+}$ (**7**, equatorial edge sharing)[27] > $[Fe_2(H_2Hbab)_2(DMF)_2(N\text{-}MeIm)]$ (**11**, axial–equatorial edge sharing) > $[Fe_2(H_2Hbab)_2(N\text{-}MeIm)_2]$ (**10**, axial–equatorial edge sharing) > $[Fe_2(Tthd)(Im)_4]^{2+}$ (**1**, equatorial edge sharing)[21] parallels the type of bridging unit (Scheme II). A notable exception is $[Fe_2(N\text{-}Et\text{-}Hptb)(OBz)]^{2+}$ (**5**), reflecting the difference in close approach between face vs edge vs vertex-shared coordination modes (Scheme II). The methylene group induced steric requirements of the N-Et-Hptb ligand in **5** restricts the close approach of the Fe^{2+} centers.[25] These Fe···Fe distances do not appear to be directly correlated with iron coordination number or Fe-μOR (Å) bond lengths but seem to parallel the Fe–O–Fe angle, a direct consequence of facial vs edge vs vertex sharing.

Visible and Infrared Spectra. The UV–vis spectrum of **11** in DMF is conspicuous owing to the absence of low energy $RO^- \rightarrow$ Fe charge-transfer bands in the visible spectrum. The observed electronic absorption spectrum is featureless in the visible region with only a shoulder observed at 312 nm (ϵ_M = 30000). This is in contrast with the lower energy transition reported for $[Fe_2(Salmp)_2]^{2+}$ (**7**, 380 nm, ϵ_M = 32100)[27] and for $[Fe_2$-

(46) Orioli, P. L. *Coord. Chem. Rev.* **1971**, *6*, 285.
(47) Jameson, G. B.; March, F. C.; Robinson, W. T.; Koon, S. S. *J. Chem. Soc., Dalton Trans.* **1978**, 185.
(48) Cini, R. *Inorg. Chim. Acta* **1983**, *73*, 147.
(49) Mukherjee, R. N.; Abrahamson, A. J.; Patterson, G. S.; Stack, T. D. P.; Holm, R. H. *Inorg. Chem.* **1988**, *27*, 2137.

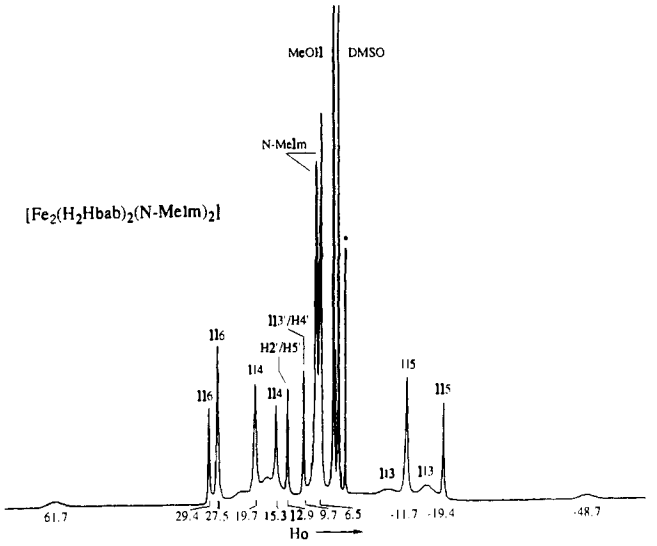

Figure 4. The 500-MHz ^{1}H NMR spectrum (70 to −60 ppm) of a 50 mM solution of **10** in DMSO-d_6 recorded at 303 K. Resonance assignments are as indicated. The * represents a solvent impurity.

$(Bpmp)(O_2CR')_2]^{2+}$ (**4**, 422 nm, ϵ_M = 2300)[24] although in the latter case, the excitation has been assigned as an $Fe^{2+} \rightarrow$ pyridine charge-transfer transition.

The presence of an amide I band ($\nu_{amideCO}$ = 1640 cm^{-1}) that is substantially unshifted from that of the uncoordinated ligand observed in both the solid state (**10**) and solution (**11**) infrared spectrum suggests that ligand coordination does not perturb the stretching frequency. In addition, $\nu_{amideNH}$ stretching vibrations are observed at 3450 cm^{-1}, indicating amide nitrogen coordination is not present.

NMR Properties. DMF or DMSO solutions of $[Fe_2(H_2Hbab)_2(N\text{-}MeIm)_2]$ are strongly paramagnetic and exhibit well-resolved isotropically shifted ^{1}H NMR spectra that span over 100 ppm in chemical shift (Figure 4). The spectrum of **10** in DMSO indicates effective 2-fold symmetry with primarily shifted N-MeIm and solvent resonances appearing between 1 and 10 ppm. The relatively narrow line widths observed ($\nu_{1/2}$ = 110 Hz) are expected for high-spin dinuclear ferrous complexes[50] and have been similarly reported for $[Fe_2(Bpmp)(O_2CR')_2]^{2+}$ (**4**)[24] and $[Fe_2(Salmp)_2]^{2+}$ (**7**).[27] Many of the sharp paramagnetically shifted resonances observed in solutions of **10** can be tentatively assigned based on relative line widths, integrations, T_1 relaxation measurements, and methyl substitution at the 3, 4, and 5 positions of the phenolate rings and the 3′/4′ position of the *o*-phenylenediammine ring.[51] Three categories of resonances were observed based on T_1 measurements: those with T_1 values between 10 and 25 ms corresponding to Fe^{2+}–proton distances of approximately 4–5.5 Å, those with T_1 values between 25 and 40 ms, corresponding to Fe^{2+}–proton distances of >5.5 Å, and those with T_1 values greater than 50 ms.

The resonances at −7.5 and −15.9 ppm are assigned as the phenolate H3 position. Owing to the broad nature of these resonances, we were unable to obtain accurate T_1 data. However, this assignment is consistent with the observation that the protons closest to the paramagnetic center are substantially broader than the others.[50,51] Methyl substitution studies and T_1 relaxation measurements allow the phenolate H4 (19.7 ppm (13 ms), 15.3 ppm (10 ms)), phenolate H5 (−11.7 ppm (35 ms), −19.4 ppm (32 ms)), and phenolate H6 (29.4 ppm (22 ms), 27.5 ppm (24 ms)) resonances to be identified. Methyl substitution studies indicated that the resonances observed at 9.7 ppm (110 ms) is one of the H3′/H4′ resonances of the *o*-phenylenediammine ring. Integration of the N-MeIm region of the spectrum (7.0 and 6.5 ppm) indicates

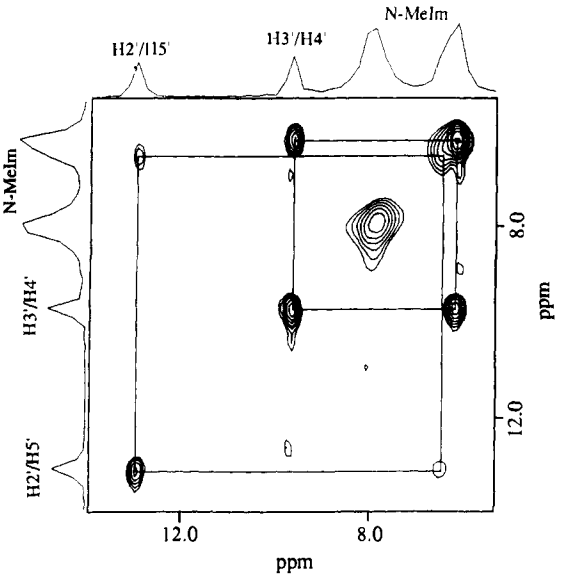

Figure 5. Enlargement of the *o*-phenylenediammine cross peak area (14–5 ppm) in the HOHAHA spectrum of **10** in DMSO-d_6 obtained with a 5-ms spin-lock time. Conditions are as described in text.

that the remaining H3′/H4′ proton is located in the resonance envelope observed at 6.5 ppm which contains the methyl groups of N-MeIm. The remaining H2′/H5′ protons were assigned to the resonances at 12.9 ppm (110 ms) and to the envelope at 6.5 ppm. Confirmation of the assignments of the *o*-phenylenediammine resonances were made by direct observation of their scalar *J* couplings detected through two-dimensional HOHAHA experiments.[38,39]

Figure 5 shows the region of the spectrum demonstrating the connectivity of the *o*-phenylenediammine portion of the spectrum. The presence of strong cross peaks are clearly observed between resonances at 12.96 and 6.21 ppm as well as between 9.70 and 6.52 ppm. These NMR data suggest that the shifts are predominantly contact in nature owing to the alternating signs around the ring systems. An NMR analysis of the dynamic properties of this complex is in progress and will be reported subsequently.

Electrochemistry. The results of cyclic voltammetry (CV) experiments performed in DMF for **11** are shown in Figure 6a. Measurements over the range +0.00 to −1.00 V versus SCE revealed two quasi-reversible redox processes at $E^1_{1/2}$ = −250 mV (ΔE_{pp} = 80 mV) and $E^2_{1/2}$ = −500 mV (ΔE_{pp} = 240 mV) at a scan rate of 100 mV s^{-1}. Ligand-centered redox behavior was observed outside this region and did not interfere with metal-based processes. Solvent systems other than DMF (CH_2Cl_2/1% DMF, CH_2Cl_2/10% DMF, CH_3CN/1% DMF) resulted in irreversible (no coupled reductive wave) behavior. Owing to the close proximity of the two redox processes, square-wave voltammetry was used to assess the nature of the quasi-reversible processes.[43] The results, shown in Figure 6b, clearly indicate that each step is a one-electron process ($E^1_{1/2}$:$E^2_{1/2}$, 1:0.9). This supports the assignment of the observed redox processes as belonging to sequential core transformations (eq 2):

$$[Fe_2(H_2Hbab)_2]^{2+} \overset{-250\ mV}{\leftrightarrow} [Fe_2(H_2Hbab)_2]^{+} \overset{-500\ mV}{\leftrightarrow} [Fe_2(H_2Hbab)_2] \quad (2)$$

The stability of the mixed-valence [Fe^{2+}, Fe^{3+}] complex can be estimated by its comproportionation constant, K_{com}, for the following equilibrium:

$$[Fe_2(H_2Hbab)_2]^{2+} + [Fe_2(H_2Hbab)_2] \overset{K_{com}}{\rightleftharpoons} 2[Fe_2(H_2Hbab)_2]^{+} \quad (3)$$

$$E^1_{1/2} - E^2_{1/2} = -0.0591 \log(K_{com})$$

From the above electrochemical data K_{com} is calculated to be 1.7 × 10^4 suggesting that the mixed-valence form is only moderately

(50) Bertini, I.; Luchinat, C. *NMR of Paramagnetic Molecules in Biological Systems*; Benjamin Cummings: Menlo Park, CA, 1986.
(51) La Mar, G. N.; Horrocks, W. DeW., Jr.; Holm, R. H. *NMR of Paramagnetic Molecules*; Academic Press; New York, 1973.

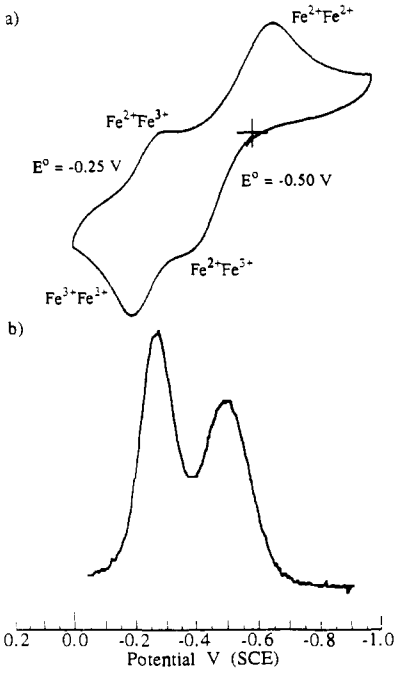

Figure 6. (a) Cyclic voltammogram of a 5 mM solution of **11** in DMF containing 0.1 M tetra-*n*-butylammonium tetrafluoroborate at 100 mV s^{-1}. Voltage readings are referenced to a Ag wire electrode. Ferrocene was added as an internal calibrant. (b) Square wave voltammogram of a 5 mM solution of **11** in DMF containing 0.1 M tetra-*n*-butylammonium tetrafluoroborate depicting two one-electron redox steps (area ratio $E^1_{1/2}$(−250 mV):$E^2_{1/2}$(−500 mV); 0.9:1.0).

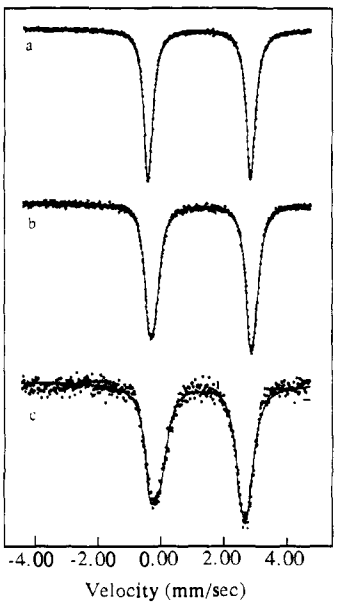

Figure 7. Mossbauer spectra of (a) polycrystalline sample of **10**, (b) polycrystalline sample of **11**, and (c) 20 mM solution of **10** in DMF, recorded at 4.2 K. The solid lines are the results of the least-squares fitting of one (a) or two (b) and (c) quadrupole doublets to the spectra. Full parameters are presented in the text.

stable. It is interesting to note that the mixed-valence form of **11** is substantially less stable than that reported for the $[Fe_2(Salmp)_2]^{2-,1-,0}$ series ($E^1_{1/2}$ = −460 mV; $E^2_{1/2}$ = −1.00 V vs SCE; K_{com} of 1.4 × 10^9).[27] Several factors may contribute to this difference, including variations in coordination donor set (NO_4 and O_6 vs N_2O_4), ligand coordination mode, and coordination geometry. The negative charge of the $[Fe_2(Salmp)_2]^{2-,1-,0}$ series, unlike the $[Fe_2(H_2Hbab)_2]^{0,1+,2+}$ series, is expected to facilitate formation of the mixed-valence and fully oxidized species. Thus, the behavior of **11** appears to be intermediate to **7**, and the $[Fe_2(Bpmp)(EtCO_2)_2]^{3+,2+,1+}$ series[24] which is reported to show redox behavior at +690 and −100 mV vs SCE. While all members of the $[Fe_2(Salmp)_2]^{2-,1-,0}$ series have been isolated and crystallographically characterized, only $[Fe_2(Bpmp)(EtCO_2)_2]^{1+,2+}$ have been structurally examined.

Repetitive CV scans of $[Fe_2(H_2Hbab)_2]$ over the range +0.00 to −1.00 V in 0.1 M TBAT/DMF show that the two redox couples are maintained with no significant decrease in either cathodic or anodic waves. There is a pronounced scan rate dependence of ΔE_p values for the $[Fe^{2+}, Fe^{2+}]/[Fe^{2+}, Fe^{3+}]$ couple ranging from ΔE_p = 170 mV (25 mV s^{-1}) to ΔE_p = 305 mV (200 mV s^{-1}), while over the same scan rate range, the $[Fe^{2+}, Fe^{3+}]/[Fe^{3+}, Fe^{3+}]$ couple shows only a modest dependence (80–100 mV). The dependence of ΔE_p vs scan rate for the $[Fe^{2+}, Fe^{2+}]/[Fe^{2+}, Fe^{3+}]$ couple, which can be attributed to kinetic effects, allowed the measurement of an intrinsic rate constant $k_s \approx 3 \times 10^{-5}$ s^{-1}, assuming pseudo-first-order kinetics. This value is thought to reflect either a reversible structural reorganization about the redox active centers, solvolysis reaction following the redox process, or the breaking or making of Fe–ligand bonds. Experiments designed to identify the role of solvent (DMF), performed in the noncoordinating solvent HMPA (hexamethylphosphoramide), were unsuccessful owing to rather large solvent resistance factors which could not be corrected for by standard techniques. The addition of 1 molar equiv of N-MeIm resulted in an increase of 50 mV for the ΔE_p of the $[Fe^{2+}, Fe^{2+}]/[Fe^{2+}, Fe^{3+}]$ couple (280–330 mV) and no significant changes in the ΔE_p of the $[Fe^{2+}, Fe^{3+}]/[Fe^{3+}, Fe^{3+}]$ couple; additional N-MeIm (2–10 equiv) had no observable effect. However, the addition of ≥25 equiv of N-MeIm resulted in increasing irreversible behavior. Furthermore, while the addition of 1–3 molar equiv of NEt_3 had no effect on either redox couple; the presence of ≥4 equiv of amine resulted in a pronounced degradation of the sample. These results suggest that neither N-MeIm substitution nor proton loss phenomena are involved in the rate-determining step of the quasi-reversible $[Fe^{2+}, Fe^{2+}]/[Fe^{2+}, Fe^{3+}]$ couple. Verification of structural reorganization will require crystallographic characterization of the mixed-valence species.

Mossbauer Spectra. Zero-field Mossbauer spectra of polycrystalline samples of **10** and **11** were measured at 4.2 and 80 K. Representative spectra are shown in Figure 7. The Mossbauer spectrum of **10** (Figure 7a) consists of a single quadrupole split doublet. Least-squares fit (solid line) to the experimental points assuming Lorentzian absorption lines gives an isomer shift δ = 1.17 (3) mm s^{-1} (relative to metallic Fe at 298 K) and a quadrupole splitting of ΔE_Q = 3.24 (5) mm s^{-1} at 80 K with δ = 1.18 (3) mm s^{-1} and ΔE_Q = 3.26 (5) mm s^{-1} at 4.2 K. The observed line widths (full width at half maximum: Γ_{80K} = 0.32 (4) mm s^{-1}, $\Gamma_{4.2K}$ = 0.34 (4) mm s^{-1}) are consistent with equivalent iron sites. Observations that the two sites have equivalent ΔE_Q values with similar temperature dependencies suggest that the two ferrous centers experience equivalent environments, consistent with the centrosymmetric structure of **10**.

However, the Mossbauer spectrum of **11** (Figure 7b) consists of two overlapping quadrupole doublets as revealed by the breadth and asymmetry of the observed signal. Simulation of the spectrum indicates two distinct Fe sites of equal population characterized by δ_1 = 1.27 (3) mm s^{-1}, ΔE_{Q1} = 3.35 (5) mm s^{-1} (Γ_1 = 0.36 (4) mm s^{-1}) and δ_2 = 1.30 (3) mm s^{-1}, ΔE_{Q2} = 3.00 (5) mm s^{-1} (Γ_2 = 0.36 mm s^{-1}) at 4.2 K and δ_1 = 1.25 (3) mm s^{-1}, ΔE_{Q1} = 3.32 (5) mm s^{-1} (Γ_1 = 0.32 (4) mm s^{-1}) and δ_2 = 1.30 (3) mm s^{-1}, ΔE_{Q2} = 3.02 (5) mm s^{-1} (Γ_2 = 0.32 mm s^{-1}) at 80 K. The observed Mossbauer parameters for polycrystalline **10** and **11** are indicative of high-spin ferrous states for both iron centers.[52] The slight increase in the quadrupole splitting as the temperature is decreased from 80 to 4.2 K is typical for high-spin ferrous systems,[52] due to changes in the Boltzman populations of the low-lying electronic states that form as a consequence of spin-orbit and low-symmetry crystal field perturbations.

(52) Dickson, D. P. E.; Berry, F. J. *Mossbauer Spectroscopy*; Cambridge University Press: Cambridge, UK, 1986.

Table III. Comparison of Structural Features of Diiron(II) Complexes[a]

property	1	2	3	4	5	7	10	11
Fe···Fe (Å)	3.117 (2)	3.32 (1)	3.5736 (8)	3.348 (1)	3.473 (7)	3.202 (2)	3.165 (7)	3.190 (4)
Fe-μOR (Å)	2.091 (4)	1.987 (8)	2.113 (2)	2.052 (1)	1.960 (6)	2.129 (7)	1.997 (7)	2.01 (1)
	2.092 (5)		2.172 (2)	2.062 (1)	1.973 (7)	2.145 (8)	2.167 (7)	2.06 (1)
						2.168 (8)		2.08 (1)
						2.195 (7)		2.22 (1)
Fe-μO,O′ (Å)	na[b]	2.142 (9)	2.039 (3)	2.035 (2)	2.017 (8)	na[b]	na[b]	na[b]
		2.12 (1)	2.094 (2)	2.045 (2)	2.056 (7)			
			2.150 (2)	2.138 (2)				
			2.162 (2)	2.150 (2)				
Fe–OR–Fe (deg)	93.3 (2)	113.2 (2)	113.0 (1)	108.93 (6)	nr[c]	95.6 (3)	98.9 (3)	97.7 (5)
						95.9 (3)		100.7 (5)
coord no.	6,6	6,6	6,5	6,6	5,5	6,6	5,5	6,5

[a] **1**,[21] $[Fe_2(Tthd)Im_4]^{2+}$; **2**,[22] $[Fe_2(Me_3Tacn)_2(OAc)_2(OH)]^+$; **3**,[23] $[Fe_2(Bipm)_2(O_2CH)_4]$; **4**,[24] $[Fe_2(Bpmp)(O_2CR')_2]^{2+}$; **5**,[25] $[Fe_2(N\text{-Et-Hptb})(OBz)]^{2+}$; **7**,[27] $[Fe_2(Salmp)_2]^{2+}$; **10**, $[Fe_2(H_2Hbab)_2(N\text{-MeIm})_2]$; **11**, $[Fe_2(H_2Hbab)_2(DMF)_2(N\text{-MeIm})]$. [b] Not applicable. [c] Not reported.

It is interesting to note that the ΔE_Q value for **10** is significantly larger than reported quadrupole splitting values (4.2 K) for six-coordinate dinuclear ferrous centers (Table IV) observed in $[Fe_2(Tthd)(1m)_4]^{2+}$ (**1**),[21] $[Fe_2(Me_3Tacn)_2(OAc)_2(OH)]^+$ (**2**),[22] $[Fe_2(Bipm)_2(O_2CH)_4]$ (site one) (**3**),[23] $[Fe_2(Bpmp)(O_2CR')_2]^{2+}$ (**4**),[24] and $[Fe_2(Tathip)]^+$ (**6**)[26] but similar to those reported for the class of five-coordinate ferrous sites of $[Fe_2(Bipm)_2(O_2CH)_4]$ (site 2, ΔE_{Q2} = 3.30 mm s^{-1}) (**3**)[23] and $[Fe_2(N\text{-Et-Hptb})(OBz)]^{2+}$ (**5**).[25] We ascribe the larger ΔE_Q value observed in polycrystalline **11** to the inherently less symmetric trigonal-bipyramidal Fe(1) site, while the smaller ΔE_Q value is thought to arise from the more symmetric octahedral Fe(2) site. Although such differences are expected for the less symmetric five-coordinate ligand environment, additional data will have to be collected prior to establishing the use of ΔE_Q values to draw structural inferences.

We have also examined the frozen solution Mossbauer spectrum of **10** (20 mM, DMF solutions) at 80 and 4.2 K (Figure 7c). At each temperature, simulation of the data indicate the presence of inequivalent ferrous centers characterized by similar chemical isomer shifts but significantly different quadrupole doublets of about equal intensity (δ_1 = 1.24 (3) mm s^{-1}, ΔE_{Q1} = 3.02 (5) mm s^{-1}, Γ_1 = 0.50 mm s^{-1}, P_1 = 62%; δ_2 = 1.28 (3) mm s^{-1}, ΔE_{Q2} = 2.46 (5) mm s^{-1}, Γ_2 = 0.50 mm s^{-1}, P_2 = 38% at 80 K; δ_1 = 1.24 (3) mm s^{-1}, ΔE_{Q1} = 3.08 (5) mm s^{-1}, Γ_1 = 0.46 mm s^{-1}, P_1 = 57%; δ_2 = 1.29 (3) mm s^{-1}, ΔE_{Q2} = 2.54 (5) mm s^{-1}, Γ_2 = 0.46 mm s^{-1}, P_2 = 43% at 4.2 K). The different ΔE_Q values establish unequivocally that the two Fe sites have different and unique environments. On the basis of the significantly different ΔE_Q values and the analysis of the Mossbauer spectra of polycrystalline **10** and **11**, we have assigned the larger quadrupole splitting of the frozen solution sample to the five-coordinate Fe(1) $FeNO_4$ site observed in the crystal structure of **11** which has a lower symmetry environment than the more symmetric six-coordinate Fe(2) FeO_6 site which is assigned the smaller quadrupole splitting value. The broadening of the absorption lines in going from the solid state to solution state may be understood in terms of either the greater disorder in ligand orientation present in the glassy phase generated upon rapid freezing of the absorber, solution dynamic properties of **11** or a combination of both phenomena.

Thus, when dissolved in DMF, **10** appears to undergo an expansion of one coordination sphere, generating a six- and five-coordinate Fe^{2+} core. Furthermore, the dominant solution species is analogous to **11** in terms of core coordination number.

Magnetic Susceptibility Properties. Measurements were performed on microcrystalline samples of **10** by SQUID susceptometry over the interval 12–300 K. Plots of molar susceptibility and effective moments versus temperature are presented in Figure 8. The two high-spin ferrous spin centers, S_1 and S_2, in **10** may either be noninteracting ($S_1 = S_2 = 2$) or interact in either an antiferromagnetic or ferromagnetic (ground state $S = S_1 + S_2$) manner. The temperature-dependent magnetic behavior was modeled using the theory of Heisenberg, Dirac, and Van Vleck for magnetic coupling in a dinuclear system.[53] No attempt was made to model either spin-orbit coupling or zero-field splitting phenomena. The temperature-dependent susceptibility expressions used in the simulations were those derived from the general isotropic exchange Hamiltonian, $\mathcal{H} = -2JS_1 \cdot S_2$, where J is the intramolecular exchange interaction. The generalized expression for the magnetic susceptibility for **10** is given by eqs 4 and 5 where $C = (Ng^2\mu_\beta^2)/(kT)$ and $x = J/(kT)$.[53] A Curie–Weiss-type term was included to correct for a paramagnetic impurity where ρ is the mole fraction of the impurity. Least-squares optimization of

$$X^M = (1 - \rho)Cf(J,T) + 4.4\rho/(T - \Theta) \quad (4)$$

$$f(J,T) = (2e^{2x} + 10e^{6x} + 28e^{12x} + 60e^{20x})/(1 + 3e^{2x} + 5e^{6x} + 7e^{12x} + 9e^{20x}) \quad (5)$$

eq 4 gave g = 2.19, J = +2.65 cm^{-1}, Θ = 11.10, and $\rho = 1.0 \times 10^{-2}$ (Figure 8). It is apparent from the temperature dependence of $1/X$ (inset Figure 8) that the magnetic description of **10** deviates from that of two independent Fe^{2+} centers. Fits to the data are significantly improved with a nonzero J value. However, owing to the complicated energy level distributions expected for situations where the magnitude of J is comparable to the magnitude of the zero-field splitting parameter D, the inclusion of D in the theoretical expression used to calculate J is required for a unique calculated fit to the data. Nonetheless, this analysis suggests the lack of significant magnetic exchange coupling between the Fe^{2+} centers in **10**.

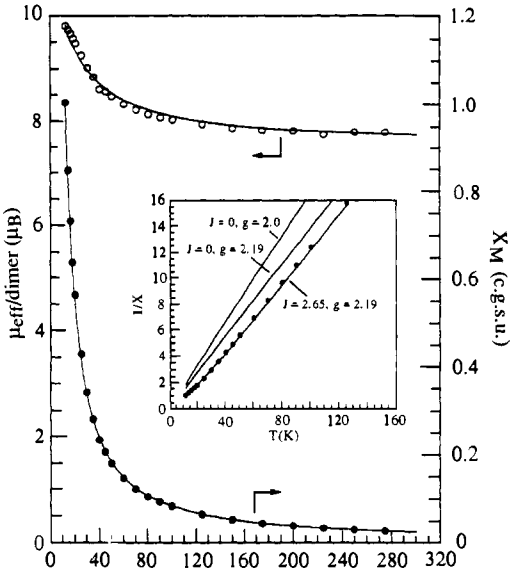

Figure 8. Plots of X_M (●) and μ_{eff} (○) vs T(12–300 K) for microcrystalline **10**. The solid line represents the best least-squares fit of eq 4 (see text) to the experimental susceptibility data. Inset: Temperature dependence of the reciprocal molar susceptibility of **10**. Spin-uncoupled behavior at g = 2.0 and g = 2.19 is shown. The remaining solid line is a theoretical fit to the data using the parameters defined in the text.

(53) O'Connor, C. J. *Progress In Inorganic Chemistry*; Lippard, S. J., Ed.; John Wiley & Sons: New York, 1982; Vol. 29, p 203.

Table IV. Spectroscopic Comparison of Diiron(II) Complexes[a]

property	1	2	3	4	5	7	10	11
redox potentials[b]								
$[Fe^{2+},Fe^{2+}] \rightarrow [Fe^{2+},Fe^{3+}]$	nr[c]	−1260	nr[c]	+120	nr[c]	−1000		−500
$[Fe^{2+},Fe^{3+}] \rightarrow [Fe^{3+},Fe^{3+}]$	nr[c]	−130	nr[c]	+800	nr[c]	−460		−250
$J(cm^{-1})$[d]	−1.5	−13.1	≈0	>0	≈−11	+1.23	≈+2.5	nr[c]
EPR	nr[c]	silent	$g \approx 16$	$g \approx 16$	nr[c]	nr[c]	nr[c]	$g \approx 12$
Mossbauer[e]								
δ (mm s^{-1})	0.739	1.16	1.25, 1.26	1.21, 1.22	1.07	nr[c]	1.18	1.27, 1.30
ΔE_Q (mm s^{-1})	2.080	2.83	3.30, 2.56	2.87, 2.52	3.13		3.26	3.35, 3.00

[a] **1**,[21] $[Fe_2(Tthd)Im_4]^{2+}$; **2**,[22] $[(Fe_2(Me_3Tacn)_2(OAc)_2(OH)]^+$; **3**,[23] $[Fe_2(Bipm)_2(O_2CH)_4]$; **4**,[24] $[Fe_2(Bpmp)(O_2CR')_2]^{2+}$; **5**,[25] $[Fe_2(N\text{-}Et\text{-}Hptb)(OBz)]^{2+}$; **7**,[27] $[Fe_2(Salmp)_2]^{2+}$; **10**, $[Fe_2(H_2Hbab)_2(N\text{-}MeIm)_2]$; **11**, $[Fe_2(H_2Hbab)_2(DMF)_2(N\text{-}MeIm)]$. [b] $E_{1/2}$ values in mV. [c] Not reported. [d] $\mathcal{H} = -2JS_1 \cdot S_2$. [e] Polycrystalline samples, 4.2 K.

Solution magnetic susceptibility measurements verify that solutions of **11** consist of high-spin Fe^{2+} centers.[41] Magnetic moments of **11** in DMF solutions measured between 263 and 298 K are in agreement with those in the solid state over the same temperature range despite the apparent substitution of one N-MeIm group by two DMF molecules. The observed value (8.09 μ_B at 298 K), which exceeds by ≈ 1 μ_B that value expected for a high-spin Fe^{2+} dimer system ($S_1 = S_2 = 2$; $\mu_{eff} = 6.93$ μ_B, $g = 2$), indicating **11** has a $g > 2$ value.

The observed absence of strong magnetic exchange interactions of **10** is interesting owing to the paucity of crystallographically defined diferrous ferromagnetic compounds (Table IV). The only established synthetic dinuclear ferrous ferromagnetic complex is **7** with $J = +1.23$ cm^{-1}.[27] The remaining crystallographically characterized diferrous complexes containing the $Fe_2(OR)_2$ core are known to be antiferromagnetic ($[Fe_2(Tthd)A_4]$; A = py, MeNic, MeIm, Im).[21] However, reports of weak ferromagnetic behavior in ligand bound forms of deoxyhemerythrin ($J = 1.7$ cm^{-1})[19,54] and MMO[9d,e] confirm the importance of ferromagnetic coupling in naturally occurring systems and argues for further examination of the structural/electronic basis of the magnetic behavior observed for **10** and **11**. We are therefore currently examining both field and temperature-dependent Mossbauer spectroscopic data and SQUID magnetization data of polycrystalline **10** and **11** and DMF solutions of **10** in order to fit the entire data set with a consistent set of Hamiltonian parameters. This work will be communicated at a future date.

EPR Spectra. Low-temperature Mossbauer spectroscopic analysis of polycrystalline and DMF solutions of **10** and **11** showed only the presence of high-spin ($S = 2$) Fe^{2+}. This result suggested that a low-field EPR signal representing an integer spin transition of the non-Kramers center would be observable.[55] Recent analysis of the fully reduced form of MMO shows an intense X-band EPR signal with zero crossing near $g = 16$, indicating that the two Fe^{2+} centers are ferromagnetically coupled.[9e]

DMF solutions of **11** show no EPR absorbances at liquid nitrogen temperatures. However, at liquid He temperatures, an intense broad signal is observed at low field with its maximum amplitude at ≈ 650 G (Figure 9). The signal at $g = 4.3$ results from oxidation of **11** during sample preparation and corresponds to less than 1% of total Fe in the sample. The shape of the low field signal is predominantly negative in sign and approaches the baseline asymptotically with increasing field. The spectrum is most intense at lowest temperatures and loses intensity quite rapidly as the temperature is increased. The signal broadens out and disappears between 30 and 40 K. No obvious power saturation effects were observed at low temperatures (7 K). The broad nature of the signal is most likely a consequence of rapid spin–lattice relaxation effects, the random orientation of the molecules and the spread in zero-field splitting parameter. Analogous broad integer spin EPR spectra have been reported for $[Fe_2(Bipm)_2(O_2CH)_4]$ (**3**)[23] and $[Fe_2(Bpmp)(O_2CR')_2]^{2+}$ (**4**)[24] which gave EPR signals at $g \approx 16$. A detailed analysis of the EPR spectrum of $[Fe_2(Bpmp)(O_2CR')_2]^{2+}$ was consistent with ferromagnetic coupling between the phenolate-bridged ferrous centers.

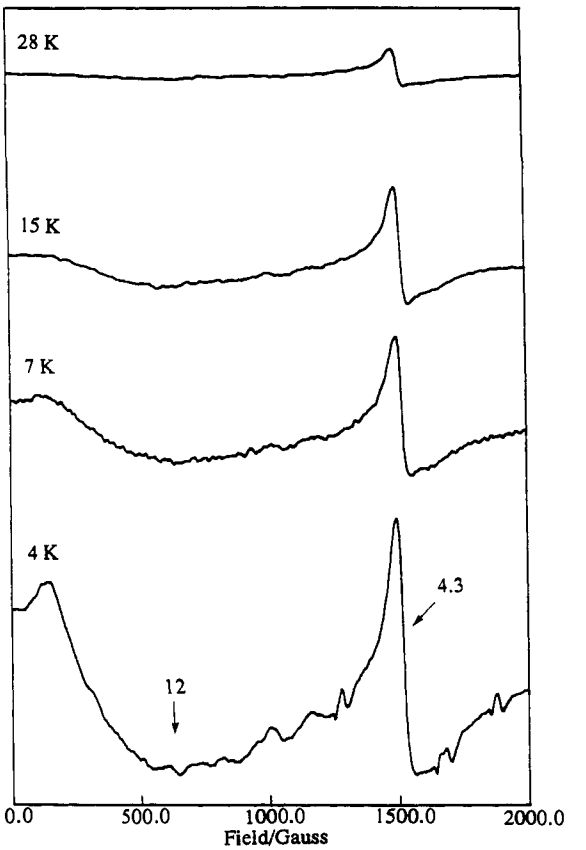

Figure 9. Variable temperature (4–28 K) X-band EPR spectra of frozen solutions of 5.0 mM **11** in DMF obtained with an observed microwave power of 5×10^{-3} mW. The signal at $g = 4.3$ is due to slight oxidation of sample (<1%). Above ≈30 K the signal broadened and disappeared.

Assessment of Model Compounds. While accurate spectroscopic and magnetic models of the dinuclear ferrous complexes found in methane monooxygenase, hemerythrin, ribonucleotide reductase, and purple acid phosphatases have been reported,[17-19] there are very few compounds that can model their chemistry owing to the difficulty of synthesizing complexes containing coordinatively unsaturated metal centers. It is therefore essential to synthesize compounds with either labile or coordinatively unsaturated Fe^{2+} centers. With the exception of structures **3**, **5**, **10**, and **11**, all complexes contain two six-coordinate ferrous atoms. Whereas **5** and **10** each consists of two approximately trigonal-bipyramidal centers, **3** and **11** each contain a five- and a six-coordinate Fe^{2+} center. These three complexes are known to react with molecular oxygen producing μ-oxo Fe^{3+} dimers in the case of **3** and **11** or the irreversible formation of a peroxo-bridged Fe^{3+} dimer as shown by low-temperature spectroscopic characterization of **5** with O_2.

While the use of the H_2Hbab^{2-} ligand was not expected to produce an accurate structural model for the active site of MMO

(54) Hendrich, M. P.; Pearce, L. L.; Que, L., Jr.; Chasteen, N. D.; Day, E. P. *J. Am. Chem. Soc.* **1991**, *113*, 3039.

(55) (a) Hagen, W. R. *Biochim. Biophys. Acta* **1982**, *708*, 82. (b) Hendrich, M. P.; DeBrunner, P. G. *J. Magn. Reson.* **1988**, *78*, 133. (c) Hendrich, M. P.; DeBrunner, P. G. *Biophys. J.* **1989**, *56*, 489.

Table V. Comparison of Spectroscopic Features of the [Fe^{2+}, Fe^{2+}] Cores of **10** and **11** with Reduced Methane Monooxygenase and Ribonucleotide Reductase

technique	MMO[a]	RR[b]	synthetic model
UV–vis[c]	280–290 nm	not reported	270–280 nm 312 nm (sh, ϵ_M = 30000)
redox potentials[d,e]	+48 mV (aqueous) −135 mV (aqueous)	not reported	−10 mV (DMF) −260 mV (DMF)
EXAFS/X-ray	unknown	unknown	d_{Fe-Fe} = 3.190 (4) Å no μ-oxo group
Mossbauer[f] frozen solution (4.2 K)	δ = 1.30 mm s^{-1} ΔE_Q = 3.14 mm s^{-1}	δ = 1.26 mm s^{-1} ΔE_Q = 3.13 mm s^{-1}	δ_1 = 1.24 mm s^{-1} ΔE_{Q1} = 3.08 mm s^{-1} δ_2 = 1.29 mm s^{-1} ΔE_{Q2} = 2.54 mm s^{-1} polycrystalline **10** δ = 1.18 mm s^{-1} ΔE_Q = 3.26 mm s^{-1} polycrystalline **11** δ_1 = 1.27 mm s^{-1} ΔE_{Q1} = 3.55 mm s^{-1} δ_2 = 1.30 mm s^{-1} ΔE_{Q2} = 3.00 mm s^{-1}
spin state[d,f,g]	ferromagnetic J small high spin Fe^{2+}	antiferromagnetic $J \approx -5$ cm^{-1} high spin Fe^{2+}	ferromagnetic $J \approx +2.5$ cm^{-1} high spin Fe^{2+}
EPR[d,f]	$g \approx 16$[d]	$g \approx 16$	$g \approx 12$

[a] MMO: methane monooxygenase from *Methylococcus capsulatus* (Bath). [b] RR: ribonucleotide reductase B2 subunit from *Escherichia coli* strain N6405/pSPS2. [c] Reference 10d. [d] Reference 9a. [e] Versus NHE; MMO values ±25 mV; model values ±10 mV. [f] MMO from *Methylobacterium sp.*, ref 9b; RRB2 ref 55. [g] MMO from *Methylosinus trichosporium* OB3b; ref 9d,e.

or RRB2, **10** and **11** nonetheless contain several important structural features that are essential for catalytic oxygen atom transfer activity.[30] The effectiveness of **11** as a catalyst is undoubtedly a consequence of either the presence of labile solvent molecules on Fe(2) or the coordinatively unsaturated nature of Fe(1).[30] In addition, the absence of a μ-oxo/hydroxo bridge minimizes possible fragmentation processes during redox cycling.

The value of compounds **10**/**11** as electronic state models for the fully reduced (active) forms of MMO and RRB2 is assessed in Table V. To date, there is only limited structural data characterizing the reduced forms of MMO and RRB2. However, EXAFS measurements of diferric MMO and mixed-valence species show Fe···Fe distances of 3.05 and 3.42 Å, respectively.[9b,c] In addition, analysis of the mixed-valence species core strongly suggests the absence of a short bridging oxo group and is consistent with a bridging OH or OR moiety. Recent crystallographic analysis of the oxidized form of RRB2 gives an $d_{Fe-Fe} \approx 3.3$ Å.[13] The model compounds **10** and **11** therefore have appropriate Fe···Fe distance for the fully reduced cores. The absence of a μ-oxo atom in the diiron(II) core is not unexpected owing to its predicted instability as a consequence of the significant increase in basicity of a μ-oxo group in an Fe^{2+}–O–Fe^{2+} environment. The use of phenolate oxygen atom bridges precludes this instability problem.

The electronic spectrum of **11** is analogous to that of reduced MMO in that both are relatively featureless above 300 nm.[10d] The shoulder at 312 nm observed in **11** is assigned as a phenolate to Fe charge transfer. This transition is unusual in that other $Fe_2(OR)_2$ core structures are highly colored as a result of a charge-transfer transition in the visible portion of the spectrum.[27] The lack of this band in MMO suggests a different core geometry in the protein.

The redox potentials exhibited by **11** are also of interest. Although numerous dinuclear iron–oxo complexes have been characterized, only a small subset demonstrate reversible or even quasi-reversible redox coupling between the [Fe^{2+}, Fe^{2+}], [Fe^{2+}, Fe^{3+}] and [Fe^{3+}, Fe^{3+}] states (Table IV). Results indicate that the synthetic oxo-bridged systems are unstable with respect to disproportionation, suggesting that $E^1_{1/2} < E^2_{1/2}$.[56] This phenomenon is also observed for several diiron μ-oxo metalloenzymes. Hemerythrin has reduction potentials of $E^1_{1/2}$ = 110 and $E^2_{1/2}$ = 310 mV vs NHE. Similarly, the mixed-valence form of RRB2 has not been observed which may indicate that $E^1_{1/2} < E^2_{1/2}$. This trend is reversed in MMO which has reduction potentials at E^1 = 48 and E^2 = −135 mV vs NHE[9f] similar to those measured for **11** in DMF solutions. Although it is not possible to directly compare the absolute values of these potentials owing to differences in solvents, the difference between the two processes are reasonably close (183 mV for MMO; 250 mV for **11**). This is in contrast to the $[Fe(Salmp)_2]^{2-,1-,0}$ series which have more negative potentials with a difference of 540 mV.[27] While both **7** and **11** contain two phenolate oxygen bridges, the Fe environments are significantly different (**7**, FeN_2O_4; **11**, $FeNO_4$, FeO_6) indicating that the structure of the core has a direct influence on the redox behavior.

Qualitatively, the magnetic properties of **10** and MMO are quite similar with both systems exhibiting weak ferromagnetic behavior with the model compound having $J \approx 2.5$ cm^{-1}.[9d,e] Any differences in core structure are therefore not reflected in the electronic coupling of the ferrous centers as determined by magnetic susceptibility measurements. The frozen solution Mossbauer spectra of **11** also bear a resemblance to those recorded for MMO and RRB2 in frozen buffer solutions. Preliminary analyses of the spectra of reduced RRB2[57] and **11** (characterized by two quadrupole split doublets with similar chemical isomer shifts but dissimilar quadrupole splitting) are consistent with heterogeneity of the Fe sites while reduced MMO is consistent with a single Fe environment. However, there is a striking resemblance between the results from *Methylosinus trichosporium* OB3b (Table V) and the less symmetric five-coordinate Fe(1) site in **11**, suggesting a similar electronic environment about the Fe center.

Further underscoring the similarities of the electronic structures of **11** and the dinuclear ferrous sites of MMO and RRB2 is the observation of an EPR spectrum originating from a state with integer electronic spin.[9e,57] The differences between the signal position observed in **11** ($g \approx 12$) with that of MMO and RRB2 (g = 16) clearly indicate differences in subtle structural details of the respective cores. However, the observation of similar signals suggests that the dinuclear ferrous centers are bridged by comparably poor mediators of antiferromagnetic coupling in both systems. Although the exact nature of this bridge in MMO is currently unknown, EXAFS, Mossbauer, and EPR data in total are consistent with a bridging OH or OR moiety. Apparently, the electronic structure resulting from the decrease in basicity of

(56) Que, L., Jr.; True, A. E. *Prog. Inorg. Chem.* **1990**, *38*, 97.

(57) Lynch, J. B.; Juarez-Garcia, C.; Munck, E.; Que, L., Jr. *J. Biol. Chem.* **1989**, *264*, 8091.

a protonated oxo group can be approximated by a bridging phenolate as found in **11**.

Conclusions. A model compound giving a reasonable approximation to the electronic properties of the reduced dinuclear active site of MMO and RRB2 has been synthesized and spectroscopically characterized. This compound represents a new member to the small number of structurally characterized [Fe^{2+}, Fe^{2+}] dimers that are ferromagnetically coupled as determined by magnetic susceptibility measurements, Mossbauer, and EPR spectroscopic studies.

More important than its representation of the electronic characteristics of the dinuclear ferrous site of MMO, however, is the ability of **11** to catalyze the transfer of an oxygen atom from PhIO to a variety of organic substrates yielding both "oxenoid"-like and radical-like products in a manner analogous to that reported for MMO and cytochrome P-450.[30] These studies reported herein represent characterization of the first dinuclear ferrous complex that has a demonstrated ability to perform catalytic atom transfer reactions. This is in contrast to the other dinuclear compounds discussed heretofore which solely represent structural/electronic models. While the FeO_6 and $FeNO_4$ coordination spheres observed in **11** are not without merit as purely structural models for the active core of MMO, the important properties of this complex reside in the presence of two labile solvent ligands in the coordination sphere of Fe(2) and its reasonableness as an electronic model for MMO. These factors no doubt permit the observed catalytic chemistry. Furthermore, this system has the favorable properties of allowing the synthesis of its mixed-vaience species and a thermally unstable intermediate formed during substrate oxygenation by the addition of an oxygen atom donor molecule to the fully reduced form.[30] The structural, electronic, and reactivity properties of these species and their relation to the chemistry of the dinuclear iron site of MMO are currently under investigation.

Acknowledgment. We thank donors of the Petroleum Research Fund, administered by the American Chemical Society, for support of this work. G.C.P. thanks the office of Naval Research for partial support. The Francis Bitter National Magnet Laboratory was supported by N.S.F. We appreciate the help of Drs. G. Brudvig, H. H. Thorp, and J. Bocarsley for assistance and discussions concerning the EPR, magnetic susceptibility, and electrochemical studies. Additionally, we appreciate the help of Dr. J. D. Ferrara of Molecular Structure Corporation and Dr. T. P. E. Auf der Heyde for discussions concerning the crystallographic analysis.

Supplementary Material Available: Tables of positional and thermal parameters, interatomic distances and special contacts involving non-hydrogen and hydrogen atoms, intramolecular bond angles and special angles involving non-hydrogen atoms, crystal data and solution refinement details, and torsion angles, stereoscopic views of **10** and **11**, magnetic susceptibility data for **10**, and Signer method data (40 pages); tables of calculated and observed structure factors (29 pages). Ordering information is given on any current masthead page.